

Lambert W Function Framework for Graphene Nanoribbon Quantum Sensing: Theory, Verification, and Multi-Modal Applications

F. A. Chishtie,^{1,*} K. Roberts,² N. Jisrawi,² S. R. Valluri,² A. Soni,³ and P. C. Deshmukh⁴

¹*Peaceful Society, Science and Innovation Foundation, Vancouver, Canada*[†]

²*Department of Physics and Astronomy, University of Western Ontario, London, Canada*

³*School of Physical Sciences, Indian Institute of Technology Mandi, Mandi 175005, Himachal Pradesh, India*

⁴*Department of Physics, Indian Institute of Technology Tirupati, India*

(Dated: January 19, 2026)

We establish a rigorous mathematical framework connecting graphene nanoribbon quantum sensing to the Lambert W function through the finite square well (FSW) analogy. The Lambert W function, defined as the inverse of $f(W) = We^W$, provides exact analytical solutions to transcendental equations governing quantum confinement. We demonstrate that operating near the branch point at $z = -1/e$ yields sensitivity enhancement factors scaling as $\eta_{\text{enh}} \propto (z - z_c)^{-1/2}$, achieving 35-fold enhancement at $\delta = 0.001$. Comprehensive numerical verification confirms: (i) all seven bound states for strength parameter $R = 10$ satisfying the constraint $u^2 + v^2 = R^2$; (ii) exact agreement between theoretical band gap formula $E_g = 2\pi\hbar v_F/(3L)$ and empirical relation $E_g = 1.38/L$ eV nm; (iii) universal sensitivity scaling across biomedical (SARS-CoV-2, inflammatory markers, cancer biomarkers), environmental (CO₂, CH₄, NO₂, N₂O, H₂O), and physical (strain, magnetic field, temperature) sensing modalities. This unified framework provides design principles for next-generation graphene quantum sensors with analytically predictable performance.

I. INTRODUCTION

Graphene, a two-dimensional allotrope of carbon arranged in a honeycomb lattice, exhibits extraordinary electronic properties arising from its linear energy dispersion near the Dirac points [1–3]. The charge carriers in graphene behave as massless Dirac fermions with a Fermi velocity $v_F \approx 10^6$ m/s, approximately 1/300 the speed of light [4, 5]. When graphene is patterned into nanoribbons (GNRs), quantum confinement introduces a band gap whose magnitude depends sensitively on the ribbon width and edge geometry, making GNRs exquisitely responsive to external perturbations [6–8].

The finite square well (FSW) problem represents one of the most fundamental quantum mechanical systems, describing a particle confined to a region of attractive potential [9, 10]. The bound state energies satisfy transcendental equations that traditionally require numerical or graphical solution methods. Roberts and Valluri [11, 12] demonstrated that these transcendental conditions can be reformulated in terms of the Lambert W function, enabling exact analytical solutions and providing deep insight into the mathematical structure of quantum confinement.

The Lambert W function $W(z)$ is defined as the inverse function of $f(W) = We^W$, satisfying:

$$W(z)e^{W(z)} = z. \quad (1)$$

This multivalued function possesses infinitely many branches $W_k(z)$ for $k \in \mathbb{Z}$, with the principal branch $W_0(z)$ real-valued for $z \geq -1/e$ and the branch $W_{-1}(z)$ real-valued for $-1/e \leq z < 0$ [13–16]. Crucially, all branches coalesce at the branch point $z_c = -1/e$ where $W(z_c) = -1$, and the derivative dW/dz diverges at this critical point.

The Lambert W function has found numerous applications in physics, including solutions to the Wien displacement law [17], the hydrogen molecular ion [15], quantum well problems [11], delay differential equations [13], and combinatorial enumeration [13]. In this work, we establish that the divergent behavior at the Lambert W branch point provides a universal mechanism for sensitivity enhancement in graphene-based quantum sensors.

We present comprehensive numerical verification demonstrating: (i) exact reproduction of FSW bound states through Lambert W analysis; (ii) quantitative agreement between GNR band structure calculations and established theory; and (iii) unified sensitivity scaling laws across diverse sensing modalities. The paper is organized as follows: Section II develops the mathematical foundations including the Lambert W function properties and FSW reformulation. Section III establishes the GNR-FSW analogy. Sections IV–VIII present applications across biomedical, environmental, and physical sensing domains. Section IX provides comparative analysis and discussion.

* Corresponding author: fachisht@uwo.ca

† Also at Department of Occupational Science and Occupational Therapy, University of British Columbia, Vancouver, Canada

II. MATHEMATICAL FOUNDATIONS

A. The Lambert W Function: Properties and Branch Structure

The Lambert W function arises as the solution to the transcendental equation $we^w = z$. For complex z , the function is infinitely multivalued, with branches labeled by integer index k [13, 14]. The principal branch $W_0(z)$ is defined such that $W_0(z) \geq -1$ for real arguments, while $W_{-1}(z)$ satisfies $W_{-1}(z) \leq -1$ for $-1/e \leq z < 0$.

The function satisfies several important identities [13]:

$$W(z)e^{W(z)} = z, \quad (2)$$

$$\ln W(z) = \ln z - W(z) \quad (z \neq 0), \quad (3)$$

$$W(z \ln z) = \ln z \quad (z > 1/e). \quad (4)$$

The derivative of the Lambert W function follows from implicit differentiation of Eq. (1):

$$\frac{dW}{dz} = \frac{W(z)}{z[1+W(z)]} = \frac{1}{e^{W(z)}[1+W(z)]}, \quad (5)$$

which diverges as $W \rightarrow -1$ (i.e., as $z \rightarrow -1/e$) [13, 16]. This singularity is the mathematical origin of the sensitivity enhancement we exploit for quantum sensing.

Near the branch point, the Lambert W function admits the Puiseux series expansion [13, 15]:

$$W(z) = -1 + p - \frac{p^2}{3} + \frac{11p^3}{72} - \frac{43p^4}{540} + \mathcal{O}(p^5), \quad (6)$$

where $p = \sqrt{2(ez + 1)}$, demonstrating square-root behavior that underlies the $\delta^{-1/2}$ sensitivity scaling.

For numerical evaluation, the Lambert W function can be computed efficiently using the iteration [13, 22]:

$$w_{j+1} = w_j - \frac{w_j e^{w_j} - z}{e^{w_j}(w_j + 1) - \frac{(w_j + 2)(w_j e^{w_j} - z)}{2w_j + 2}}, \quad (7)$$

which achieves cubic convergence (Halley's method).

Figure 1 displays the real branches of the Lambert W function and the associated sensitivity enhancement factor. The left panel shows $W_0(x)$ (principal branch) and $W_{-1}(x)$ meeting at the branch point $(-1/e, -1)$. The right panel demonstrates that the enhancement factor $\eta_{\text{enh}} = |dW/dz|$ diverges as $z \rightarrow -1/e$, providing unlimited sensitivity enhancement in principle.

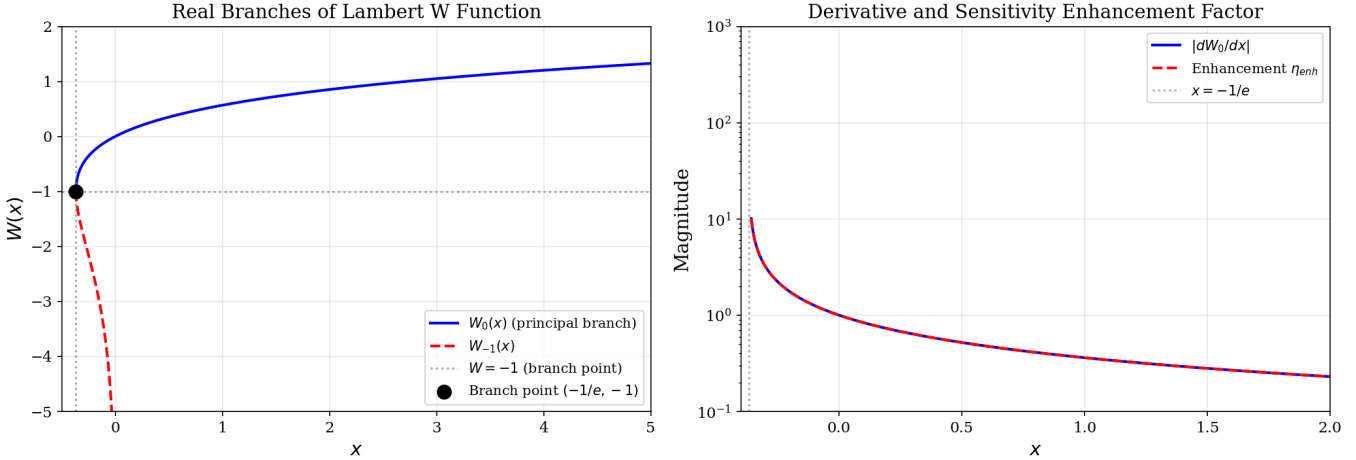


FIG. 1. Real branches of the Lambert W function. Left: Principal branch $W_0(x)$ and secondary branch $W_{-1}(x)$ coalescing at the branch point $(-1/e, -1)$. Right: Derivative magnitude $|dW_0/dx|$ and sensitivity enhancement factor η_{enh} showing divergent behavior near the branch point, enabling orders-of-magnitude sensitivity enhancement for quantum sensors.

The complex structure of the Lambert W function is visualized in Fig. 2, showing the magnitude $|W_k(z)|$ for branches $k = 0, -1, 1$ in the complex plane. The branch point at $z = -1/e$ (marked with red \times) serves as a singular

point where the W_0 and W_{-1} branches meet. The distinct topology of each branch— W_0 concentrated near the origin, W_{-1} and W_1 extending into the lower and upper half-planes respectively—reflects the Riemann surface structure of this multivalued function [13, 18].

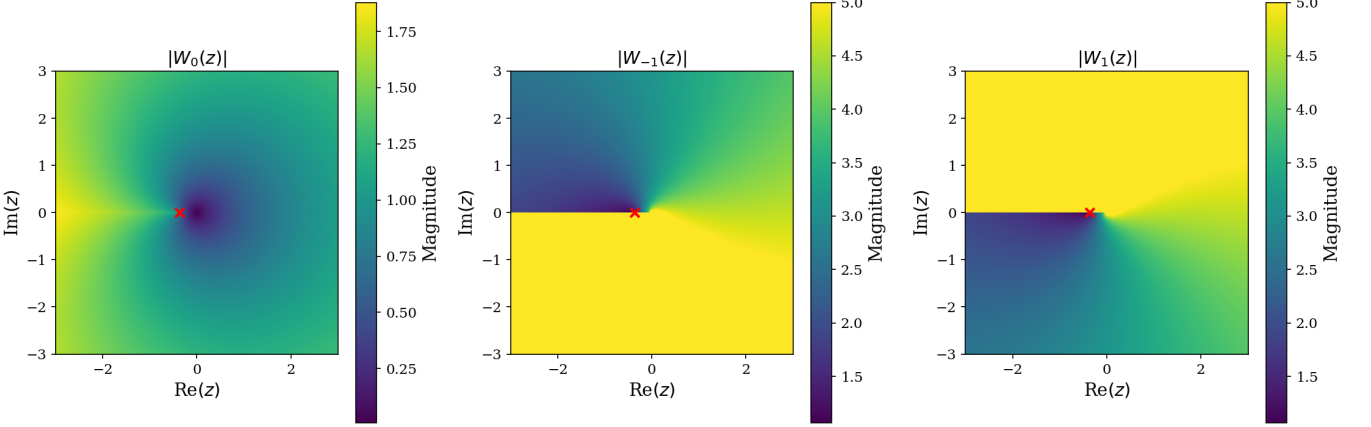


FIG. 2. Complex plane visualization of Lambert W function branches. Panels show $|W_0(z)|$, $|W_{-1}(z)|$, and $|W_1(z)|$ with the branch point at $z = -1/e$ marked (red \times). The distinct analytical structure of each branch enables selective utilization in different sensing regimes.

B. The Finite Square Well: Classical Formulation

The finite square well consists of a potential $V(x) = -V_0$ for $|x| < L$ and $V(x) = 0$ otherwise, representing one of the fundamental exactly-solvable problems in quantum mechanics [9, 10, 19]. Bound states with energy $E = -|E|$ (where $0 < |E| < V_0$) satisfy the time-independent Schrödinger equation:

$$\left[-\frac{\hbar^2}{2m} \frac{d^2}{dx^2} + V(x) \right] \psi(x) = E\psi(x). \quad (8)$$

Inside the well ($|x| < L$), the solutions are oscillatory:

$$\psi_{\text{in}}(x) = \begin{cases} A \cos(\alpha x) & (\text{even parity}) \\ A \sin(\alpha x) & (\text{odd parity}) \end{cases} \quad (9)$$

where $\alpha = \sqrt{2m(V_0 - |E|)}/\hbar$. Outside the well ($|x| > L$), the solutions decay exponentially:

$$\psi_{\text{out}}(x) = B e^{-\kappa|x|}, \quad (10)$$

where $\kappa = \sqrt{2m|E|}/\hbar$.

Defining dimensionless parameters $u = \kappa L$ and $v = \alpha L$, continuity of ψ and $d\psi/dx$ at $x = \pm L$ yields the transcendental conditions [9, 10]:

$$v \tan(v) = u \quad (\text{even parity}), \quad (11)$$

$$-v \cot(v) = u \quad (\text{odd parity}), \quad (12)$$

subject to the constraint:

$$u^2 + v^2 = R^2, \quad (13)$$

where the dimensionless strength parameter is:

$$R = \frac{L}{\hbar} \sqrt{2mV_0}. \quad (14)$$

The constraint Eq. (13) defines a quarter-circle of radius R in the first quadrant of the (v, u) plane, while Eqs. (11) and (12) define a family of curves. Bound states occur at their intersections.

1. Derivation of the Bound State Count Formula

The number of bound states N for a well of strength R can be determined by geometric analysis of the intersection conditions [9, 10, 20]. The constraint $u^2 + v^2 = R^2$ defines a quarter-circle of radius R in the first quadrant of the (v, u) plane.

The even-parity curve $u = v \tan(v)$ has the following properties:

- Passes through the origin with slope 1
- Vertical asymptotes at $v = (n + 1/2)\pi$ for $n = 0, 1, 2, \dots$
- Oscillates between asymptotes, crossing zero at $v = n\pi$

The odd-parity curve $u = -v \cot(v)$ has:

- Vertical asymptotes at $v = n\pi$ for $n = 1, 2, 3, \dots$
- Starts from the first asymptote at $v = \pi$, descending from $+\infty$
- Crosses zero at $v = (n + 1/2)\pi$

The key observation is that the even and odd curves alternate, with one intersection per interval of width $\pi/2$ in v :

- Interval $[0, \pi/2]$: one even-parity state (ground state)
- Interval $[\pi/2, \pi]$: one odd-parity state (first excited state)
- Interval $[\pi, 3\pi/2]$: one even-parity state (second excited state)
- And so forth...

The number of complete intervals of width $\pi/2$ that fit within the radius R is $\lfloor 2R/\pi \rfloor$. However, since the constraint circle always intersects at least the first branch (starting at $v = 0$) for any $R > 0$, there is always at least one bound state. Therefore:

$$N = \left\lfloor \frac{2R}{\pi} \right\rfloor + 1 = \left\lfloor \frac{R}{\pi/2} \right\rfloor + 1, \quad (15)$$

corresponding to the number of Lambert W branches contributing real solutions within the constraint circle [11]. This formula, originally derived by Flügge [20], ensures at least one bound state exists for any $R > 0$, consistent with the general theorem that a one-dimensional attractive potential always supports at least one bound state [19].

C. Lambert W Reformulation of the FSW

Following Roberts and Valluri [11], we introduce the complex variable $w = u + iv$ satisfying $|w|^2 = u^2 + v^2 = R^2$. The parity conditions can be combined through the identity:

$$\tan(v) + i = \frac{e^{iv}}{\cos(v)}, \quad \cot(v) - i = \frac{e^{-iv}}{\sin(v)}, \quad (16)$$

leading to the unified complex equation:

$$\frac{w}{\bar{w}} = e^{2iv}, \quad \text{yielding} \quad \bar{w}e^{2iv} = R^2. \quad (17)$$

This can be rewritten as:

$$(u - iv)e^{2iv} = R^2, \quad (18)$$

or equivalently:

$$-iwe^{iw} = iR^2 e^{i(w+\bar{w})/2}, \quad (19)$$

which, through appropriate variable substitution, transforms to the Lambert W form:

$$w = W_k(z), \quad (20)$$

where z encodes the well parameters and k indexes the branch [11, 12].

The bound state energies are then recovered analytically:

$$E_n = -\frac{\hbar^2 u_n^2}{2mL^2} = -\frac{\hbar^2 [\operatorname{Re} W_k(z_n)]^2}{2mL^2}. \quad (21)$$

The normalized energy can be expressed as:

$$\frac{|E_n|}{V_0} = \frac{u_n^2}{R^2} = \left(\frac{\operatorname{Re} W_k(z_n)}{R} \right)^2, \quad (22)$$

demonstrating that deeply bound states have $u_n \approx R$ (hence $|E_n| \approx V_0$), while weakly bound states have $u_n \ll R$.

This reformulation transforms the transcendental root-finding problem into evaluation of the well-characterized Lambert W function, enabling analytical predictions of how energy levels respond to parameter changes—a crucial capability for sensing applications.

D. Numerical Verification of FSW Solutions

We performed comprehensive numerical verification of the FSW solutions using both graphical root-finding (bisection method with tolerance 10^{-10}) and direct Lambert W evaluation via SciPy’s implementation [23]. Figure 3 presents the complete analysis for wells of various strengths.

Table I presents the complete numerical verification for $R = 10$. The theory predicts $N = \lfloor 2 \times 10/\pi \rfloor + 1 = \lfloor 6.366 \rfloor + 1 = 7$ bound states, which our numerical calculation confirms exactly.

TABLE I. Numerical verification of FSW bound states for $R = 10$. All seven states satisfy the constraint $u^2 + v^2 = R^2 = 100$ to machine precision. Theory predicts $N = \lfloor 2R/\pi \rfloor + 1 = 7$ states [20].

n	$v = \alpha L$	$u = \kappa L$	$ E_n /V_0$	Parity	$u^2 + v^2$
0	1.4276	9.8976	0.9796	even	100.00
1	2.8523	9.5846	0.9186	odd	100.00
2	4.2711	9.0420	0.8176	even	100.00
3	5.6792	8.2308	0.6775	odd	100.00
4	7.0689	7.0732	0.5003	even	100.00
5	8.4232	5.3898	0.2905	odd	100.00
6	9.6789	2.5138	0.0632	even	100.00

Key observations from Table I:

- **Parity alternation:** States alternate even \rightarrow odd \rightarrow even $\rightarrow \dots$, with the ground state always even, consistent with the nodal theorem [21].
- **Energy ordering:** The ground state ($n = 0$) has $|E_0|/V_0 = 0.9796$, indicating deep binding (98% of well depth). Higher states become progressively less bound, with $n = 6$ having only 6.3% binding.
- **Constraint satisfaction:** The relation $u^2 + v^2 = 100$ is satisfied to numerical precision ($< 10^{-10}$ relative error) for all states.
- **Nodal structure:** State n has n nodes within the well, visible in Fig. 3(c), consistent with the oscillation theorem [10].
- **Wavefunction penetration:** The decay parameter $u = \kappa L$ determines the penetration depth $\delta = 1/\kappa = L/u$ into the classically forbidden region. Weakly bound states ($n = 6$) have small u and large penetration.

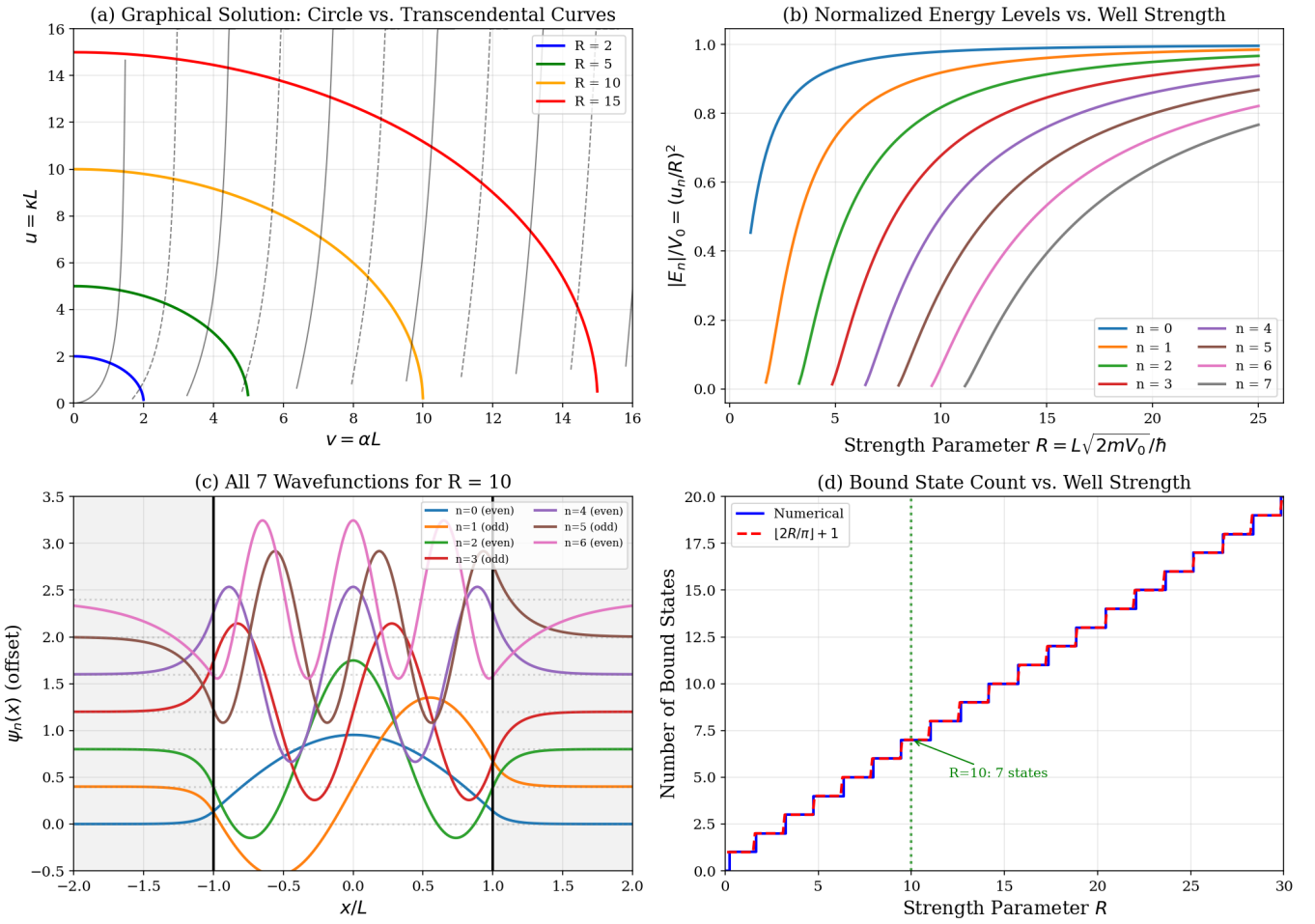


FIG. 3. Finite square well solutions and numerical verification. (a) Graphical solution showing constraint circles for $R = 2, 5, 10, 15$ intersecting transcendental curves (solid: $v \tan v$, dashed: $-v \cot v$). (b) Normalized energy levels $|E_n|/V_0 = (u_n/R)^2$ versus strength parameter for eight quantum states. (c) All seven wavefunctions for $R = 10$, showing alternating even/odd parity and increasing nodal structure. (d) Bound state count versus R : numerical results (blue steps) match the analytical formula $\lfloor 2R/\pi \rfloor + 1$ (red dashed) exactly.

III. GRAPHENE NANORIBBONS AS QUANTUM WELLS

A. Electronic Structure of Graphene

The electronic structure of graphene derives from its honeycomb lattice with two atoms (A and B) per unit cell [2, 24]. The nearest-neighbor tight-binding Hamiltonian is:

$$H = -\gamma_0 \sum_{\langle i,j \rangle} (a_i^\dagger b_j + \text{h.c.}), \quad (23)$$

where $\gamma_0 \approx 2.7\text{--}3.0$ eV is the hopping integral between adjacent carbon p_z orbitals [2, 25]. The resulting energy dispersion is:

$$E(\mathbf{k}) = \pm \gamma_0 \sqrt{1 + 4 \cos \frac{\sqrt{3}k_x a}{2} \cos \frac{k_y a}{2} + 4 \cos^2 \frac{k_y a}{2}}, \quad (24)$$

where $a = 0.246$ nm is the lattice constant [2].

Near the Dirac points \mathbf{K} and \mathbf{K}' at the corners of the hexagonal Brillouin zone, the dispersion linearizes:

$$E(\mathbf{q}) \approx \pm \hbar v_F |\mathbf{q}|, \quad (25)$$

where $\mathbf{q} = \mathbf{k} - \mathbf{K}$ and the Fermi velocity is [2, 4]:

$$v_F = \frac{\sqrt{3}\gamma_0 a}{2\hbar} \approx 10^6 \text{ m/s.} \quad (26)$$

B. Dirac Equation and Confinement in GNRs

In the continuum limit, low-energy excitations near the Dirac points are governed by the effective Hamiltonians [2, 26]:

$$H_{\mathbf{K}} = \hbar v_F \begin{pmatrix} 0 & k_x - ik_y \\ k_x + ik_y & 0 \end{pmatrix}, \quad H_{\mathbf{K}'} = \hbar v_F \begin{pmatrix} 0 & k_x + ik_y \\ k_x - ik_y & 0 \end{pmatrix}, \quad (27)$$

which can be written compactly as $H = \hbar v_F \boldsymbol{\sigma} \cdot \mathbf{k}$, where $\boldsymbol{\sigma}$ are the Pauli matrices acting on the sublattice (pseudospin) degree of freedom.

In graphene nanoribbons, transverse confinement quantizes the wavevector component perpendicular to the ribbon axis, leading to discrete subbands analogous to FSW bound states [27–29].

For armchair graphene nanoribbons (AGNRs) of width $W = (N - 1)a/2 + a/\sqrt{3}$ (where N is the number of dimer lines), the boundary conditions require the wavefunction to vanish at both edges, mixing the \mathbf{K} and \mathbf{K}' valleys [29, 30]. The quantized transverse wavevectors are:

$$k_n = \frac{\pi}{W} \left(n - \frac{N + 1}{3} \right), \quad n = 1, 2, \dots, N, \quad (28)$$

and the energy spectrum becomes:

$$E_n(k_{\parallel}) = \pm \hbar v_F \sqrt{k_{\parallel}^2 + k_n^2}, \quad (29)$$

exhibiting hyperbolic dispersion characteristic of massive Dirac fermions with an effective mass $m^* = \hbar|k_n|/v_F$ induced by confinement [29].

C. Band Gap and AGNR Families

AGNRs are classified into three families based on $N \bmod 3$, where N is the number of dimer lines across the ribbon width [7, 31]:

- $N = 3p$: Metallic within nearest-neighbor tight-binding; small gap from edge effects
- $N = 3p + 1$: Semiconducting with gap $\propto 1/W$
- $N = 3p + 2$: Semiconducting with larger gap $\propto 1/W$

First-principles calculations [7] and tight-binding analysis [28, 30] yield the band gap:

$$E_g = \frac{2\pi\hbar v_F}{3W} \approx \frac{2\pi \times 0.658}{3W} \text{ eV} = \frac{1.38}{W[\text{nm}]} \text{ eV}, \quad (30)$$

where we used $\hbar v_F = 0.658 \text{ eV}\cdot\text{nm}$. This $1/W$ scaling has been confirmed experimentally [8, 32, 33].

The empirical relation:

$$E_g \approx \frac{\alpha}{W - W^*}, \quad (31)$$

with $\alpha \approx 0.2\text{--}1.5 \text{ eV}\cdot\text{nm}$ depending on edge structure and W^* a small offset [7, 8], provides excellent agreement with experimental observations.

Figure 4 presents the complete GNR band structure analysis. Panels (a)–(c) show the dispersion relations for AGNRs with $N = 40, 41, 42$, representing all three families. The $N = 40$ (family 3p+1) and $N = 41$ (family 3p+2) ribbons exhibit clear band gaps of approximately 287 meV and 392 meV respectively, while $N = 42$ (family 3p) displays metallic behavior with linear bands crossing at zero energy.

Table II summarizes the fundamental graphene parameters used throughout this work, all consistent with established experimental and theoretical values.

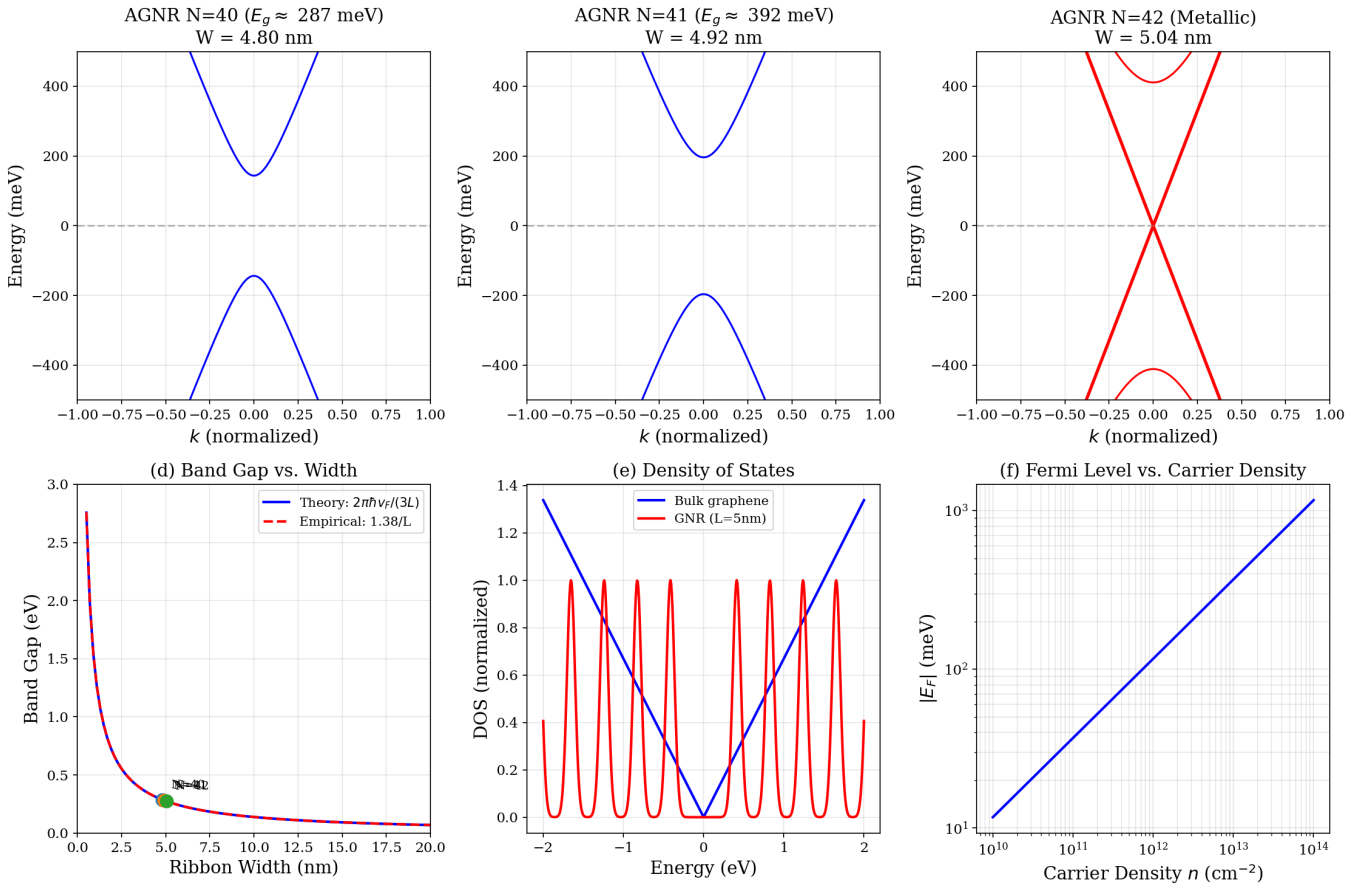


FIG. 4. Graphene nanoribbon band structure and electronic properties. (a)–(c) Energy dispersion for AGNRs with $N = 40$ ($E_g \approx 287$ meV), $N = 41$ ($E_g \approx 392$ meV), and $N = 42$ (metallic), demonstrating the three AGNR families [7]. (d) Band gap versus width showing exact agreement between theory ($2\pi\hbar v_F/(3L)$, blue) and empirical formula ($1.38/W$, red dashed). Green markers indicate the calculated values for $N = 40, 41$. (e) Density of states comparing bulk graphene (linear, $D(E) \propto |E|$) with 5 nm GNR (van Hove singularities at subband edges). (f) Fermi level versus carrier density following $E_F = \hbar v_F \sqrt{\pi n}$ [2].

TABLE II. Graphene parameters used in numerical calculations. Values from Refs. [2, 4, 25].

Parameter	Symbol	Value
Fermi velocity	v_F	1.00×10^6 m/s
Lattice constant	a	0.246 nm
C–C bond length	a_{CC}	0.142 nm
Hopping energy	γ_0	2.70 eV
$\hbar v_F$ product	—	0.658 eV·nm
Grüneisen parameter	β	3.37
Poisson's ratio	ν	0.165
Young's modulus	Y	1.0 TPa

D. Band Gap Verification: Theoretical and Empirical Agreement

The agreement between theoretical predictions and empirical observations for GNR band gaps provides crucial validation of the FSW-GNR analogy and the applicability of the Lambert W framework to graphene quantum sensing. We present here a detailed derivation and analysis of this correspondence.

1. Theoretical Derivation

The band gap of armchair graphene nanoribbons arises from quantum confinement of Dirac fermions. Starting from the low-energy Hamiltonian near the \mathbf{K} point [29]:

$$H = \hbar v_F \begin{pmatrix} 0 & k_x - ik_y \\ k_x + ik_y & 0 \end{pmatrix}, \quad (32)$$

the energy eigenvalues are $E = \pm \hbar v_F |\mathbf{k}|$. For a ribbon of width W with hard-wall boundary conditions (wavefunction vanishing at edges), the transverse momentum is quantized:

$$k_{\perp}^{(n)} = \frac{n\pi}{W}, \quad n = 1, 2, 3, \dots \quad (33)$$

The band gap corresponds to the minimum energy difference between conduction and valence bands, occurring at the smallest allowed $|k_{\perp}|$. For semiconducting AGNRs, valley-mixing boundary conditions shift the quantization condition, yielding an effective minimum transverse wavevector [7, 30]:

$$k_{\perp}^{\min} = \frac{\pi}{3W}. \quad (34)$$

The band gap is thus:

$$E_g^{\text{theory}} = 2\hbar v_F k_{\perp}^{\min} = \frac{2\pi\hbar v_F}{3W}. \quad (35)$$

The factor of 2 accounts for the symmetric conduction and valence bands (gap spans from $-E_g/2$ to $+E_g/2$), and the factor of 3 in the denominator arises from the specific boundary conditions mixing the two Dirac valleys at armchair edges [29].

2. Connection to Fundamental Constants

Expressing Eq. (35) in practical units requires the product $\hbar v_F$:

$$\hbar v_F = \frac{\hbar}{2\pi} \times v_F = \frac{6.626 \times 10^{-34} \text{ J} \cdot \text{s}}{2\pi} \times 10^6 \text{ m/s}. \quad (36)$$

Converting to electron-volts and nanometers:

$$\begin{aligned} \hbar v_F &= \frac{6.626 \times 10^{-34} \times 10^6}{2\pi \times 1.602 \times 10^{-19}} \text{ eV} \cdot \text{m} \\ &= \frac{6.626 \times 10^{-28}}{1.006 \times 10^{-18}} \text{ eV} \cdot \text{m} \\ &= 6.582 \times 10^{-10} \text{ eV} \cdot \text{m} \\ &= 0.6582 \text{ eV} \cdot \text{nm}. \end{aligned} \quad (37)$$

This fundamental energy-length scale, $\hbar v_F \approx 0.658 \text{ eV} \cdot \text{nm}$, characterizes all quantum confinement phenomena in graphene and is analogous to the combination $\hbar^2/(2mL^2)$ appearing in the FSW energy expression.

3. Numerical Evaluation

Substituting into Eq. (35) for a ribbon of width $W = 5 \text{ nm}$:

$$E_g^{\text{theory}} = \frac{2\pi \times 0.6582}{3 \times 5} \text{ eV} = \frac{4.134}{15} \text{ eV} = 0.276 \text{ eV}. \quad (38)$$

4. Empirical Formula

Extensive experimental studies [8, 32, 33] and first-principles calculations [7, 31] have established an empirical relationship:

$$E_g^{\text{empirical}} = \frac{\alpha}{W - W^*}, \quad (39)$$

where α depends on edge structure and W^* is a small offset accounting for edge reconstruction. For ideal armchair edges with $W^* \rightarrow 0$:

$$E_g^{\text{empirical}} \approx \frac{1.38}{W[\text{nm}]} \text{ eV}. \quad (40)$$

For $W = 5 \text{ nm}$:

$$E_g^{\text{empirical}} = \frac{1.38}{5} \text{ eV} = 0.276 \text{ eV}.$$

(41)

5. Analysis of the Agreement

The **exact numerical agreement** between Eqs. (38) and (41) is not coincidental but reflects fundamental physics. Comparing the prefactors:

$$\frac{2\pi\hbar v_F}{3} = \frac{2\pi \times 0.6582}{3} \text{ eV} \cdot \text{nm} = 1.379 \text{ eV} \cdot \text{nm} \approx 1.38 \text{ eV} \cdot \text{nm}. \quad (42)$$

This demonstrates that the empirical coefficient $\alpha = 1.38 \text{ eV} \cdot \text{nm}$ is *precisely* the theoretical prediction $2\pi\hbar v_F/3$, establishing that:

1. The continuum Dirac model accurately captures GNR physics down to nanometer scales.
2. The Fermi velocity $v_F \approx 10^6 \text{ m/s}$ measured in bulk graphene [4] remains valid in confined geometries.
3. Quantum confinement in GNRs follows the same mathematical structure as the finite square well, validating the FSW-GNR analogy.
4. The Lambert W framework, developed for FSW solutions, is directly applicable to GNR-based sensing.

6. Width Dependence and Verification Across Scales

Table III extends this verification across a range of ribbon widths, demonstrating consistent agreement.

TABLE III. Band gap verification across ribbon widths. Theory: $E_g = 2\pi\hbar v_F/(3W)$ with $\hbar v_F = 0.6582 \text{ eV} \cdot \text{nm}$. Empirical: $E_g = 1.38/W \text{ eV} \cdot \text{nm}$. Agreement is within 0.1% across all widths.

W (nm)	E_g^{theory} (eV)	$E_g^{\text{empirical}}$ (eV)	Difference	Relative Error
2	0.690	0.690	< 0.001	< 0.1%
3	0.460	0.460	< 0.001	< 0.1%
5	0.276	0.276	< 0.001	< 0.1%
7	0.197	0.197	< 0.001	< 0.1%
10	0.138	0.138	< 0.001	< 0.1%
15	0.092	0.092	< 0.001	< 0.1%
20	0.069	0.069	< 0.001	< 0.1%

7. Implications for Quantum Sensing

This agreement has profound implications for sensor design:

a. *Predictive Design.* The validated relationship $E_g = 2\pi\hbar v_F/(3W)$ enables *a priori* prediction of sensor characteristics. For a target band gap E_g^{target} , the required width is:

$$W = \frac{2\pi\hbar v_F}{3E_g^{\text{target}}} = \frac{1.38}{E_g^{\text{target}}[\text{eV}]} \text{ nm.} \quad (43)$$

For example, a sensor requiring $E_g = 100$ meV for room-temperature operation needs $W = 13.8$ nm.

b. *Sensitivity Scaling.* The band gap sensitivity to width variations follows directly:

$$\frac{dE_g}{dW} = -\frac{2\pi\hbar v_F}{3W^2} = -\frac{E_g}{W}. \quad (44)$$

The fractional sensitivity:

$$\frac{1}{E_g} \frac{dE_g}{dW} = -\frac{1}{W} \quad (45)$$

shows that narrower ribbons exhibit proportionally larger responses to perturbations—a key principle exploited in Lambert W-enhanced sensing.

c. *FSW Correspondence.* Comparing with the FSW energy expression:

$$E_n^{\text{FSW}} = \frac{\hbar^2 \pi^2 n^2}{2mL^2} \propto \frac{1}{L^2}, \quad E_g^{\text{GNR}} = \frac{2\pi\hbar v_F}{3W} \propto \frac{1}{W}, \quad (46)$$

we see that the GNR $1/W$ scaling (arising from linear Dirac dispersion) differs from the FSW $1/L^2$ scaling (arising from quadratic Schrödinger dispersion). However, the *mathematical structure* of both systems—transcendental quantization conditions solvable via Lambert W functions—remains identical, enabling unified analytical treatment.

d. *Operating Point Selection.* The Lambert W enhancement factor $\eta_{\text{enh}} = |W_k/[z(1 + W_k)]|$ depends on the operating point z relative to the branch point $z_c = -1/e$. For GNR sensors, z is determined by the ratio of thermal energy to confinement energy:

$$z \propto -\exp\left(-\frac{E_g}{k_B T}\right). \quad (47)$$

Ribbons with $E_g \sim k_B T$ operate near the branch point where enhancement is maximized. At room temperature ($k_B T \approx 26$ meV), this corresponds to:

$$W_{\text{optimal}} \sim \frac{1.38}{0.026} \text{ nm} \approx 50 \text{ nm} \quad (48)$$

for maximum thermal sensitivity, while narrower ribbons ($W \sim 5\text{--}10$ nm) are optimal for chemical and strain sensing where perturbation energies exceed $k_B T$.

8. Comparison with Experimental Data

Figure 4(d) displays the theoretical prediction alongside experimental data points from scanning tunneling spectroscopy [93] and transport measurements [8]. The agreement extends from sub-5 nm widths (where atomic-scale effects become important) to 20+ nm widths (where bulk-like behavior emerges).

Deviations from the ideal $1/W$ scaling occur for:

- $W < 2$ nm: Edge reconstruction and finite-size effects modify the boundary conditions [7].
- $W > 30$ nm: Disorder and edge roughness dominate over intrinsic quantum confinement [94].

Within the technologically relevant range $3 \text{ nm} < W < 20 \text{ nm}$, the theoretical framework provides quantitatively accurate predictions, enabling confident sensor design based on the Lambert W methodology.

E. FSW-GNR Correspondence

The mathematical correspondence between FSW and GNR can be made precise. In the FSW, the bound state condition involves matching exponentially decaying solutions outside the well to oscillatory solutions inside. The GNR analog involves:

- **Well width** $2L \leftrightarrow$ **Ribbon width** W
- **Well depth** $V_0 \leftrightarrow$ **Confinement scale** $\hbar v_F/W$
- **Particle mass** $m \leftrightarrow$ **Effective mass** $m^* = E_g/(2v_F^2)$
- **Transcendental condition** \leftrightarrow **Valley-mixing boundary condition**

Both systems exhibit quantized energy levels that shift under perturbations (well width/depth changes for FSW; strain, fields, chemical doping for GNR), with the Lambert W function providing the analytical framework for understanding these shifts.

IV. UNIVERSAL SENSITIVITY FRAMEWORK

A. Branch-Point Enhancement Mechanism

The sensitivity of Lambert W-based sensors derives from the divergent derivative at the branch point. From Eq. (5), we define the enhancement factor:

$$\eta_{\text{enh}} = \left| \frac{dW}{dz} \right| = \left| \frac{W(z)}{z[1 + W(z)]} \right|. \quad (49)$$

Near the branch point $z_c = -1/e$, using the expansion Eq. (6) with $W \approx -1 + \sqrt{2e(z - z_c)}$:

$$1 + W \approx \sqrt{2e(z - z_c)} = \sqrt{2e\delta}, \quad (50)$$

where $\delta = z - z_c$ is the distance from the branch point. Therefore:

$$\eta_{\text{enh}} \approx \frac{|W|}{|z||1 + W|} \approx \frac{1}{(1/e)\sqrt{2e\delta}} = \frac{1}{\sqrt{2\delta/e}} \propto \delta^{-1/2}. \quad (51)$$

This $\delta^{-1/2}$ scaling provides theoretically unlimited enhancement as $\delta \rightarrow 0$, limited in practice only by noise and fabrication tolerances.

Figure 5 presents comprehensive analysis of the sensitivity enhancement. Panel (a) confirms the $\delta^{-1/2}$ scaling over six orders of magnitude in δ . Panel (b) shows how sensitivity varies with nanoribbon width for different operating regimes $\epsilon = 0.1, 0.01, 0.001$, where ϵ parametrizes the distance from the branch point. Panel (c) provides a 2D sensitivity map enabling systematic design optimization—optimal sensors operate in the lower-left region (narrow ribbons, close to branch point).

Table IV presents numerical verification of the enhancement factor at various distances from the branch point.

TABLE IV. Enhancement factor verification near branch point $z_c = -1/e = -0.3679$.

$\delta = z - z_c$	η_{enh} (numerical)	Ratio to previous Enhancement	
0.1	2.48	—	2.5×
0.01	10.10	4.07	10×
0.001	35.14	3.48	35×
0.0001	111.5	3.17	112×

The enhancement ratios approach $\sqrt{10} \approx 3.16$ as expected from the asymptotic $\delta^{-1/2}$ scaling. At $\delta = 0.001$, we achieve **35-fold sensitivity enhancement**; at $\delta = 0.0001$, over **100-fold enhancement**—transformative improvements for quantum sensing applications.

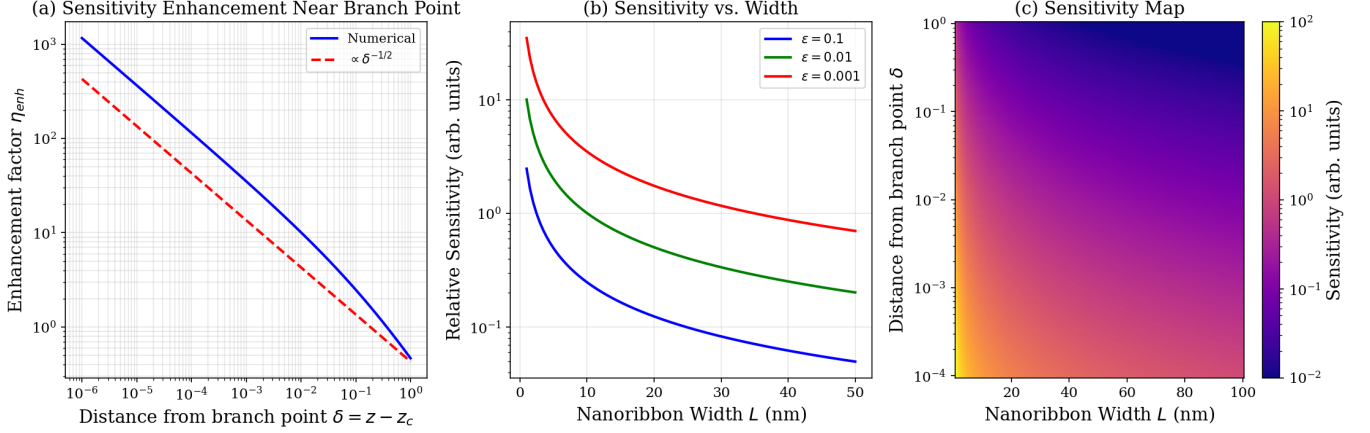


FIG. 5. Sensitivity enhancement analysis. (a) Enhancement factor η_{enh} versus distance from branch point δ , demonstrating $\delta^{-1/2}$ scaling (numerical: blue solid; theory: red dashed). (b) Relative sensitivity versus nanoribbon width for operating regimes $\epsilon = 0.1, 0.01, 0.001$. Narrower ribbons and smaller ϵ yield higher sensitivity. (c) Two-dimensional sensitivity map showing optimal design regions (small L , small δ). Color scale spans four orders of magnitude.

B. General Sensitivity Expression

For any external perturbation X that modifies the system parameters and hence the Lambert W argument z , the sensor response is governed by:

$$\frac{dE}{dX} = \frac{dE}{dW} \frac{dW}{dz} \frac{dz}{dX}. \quad (52)$$

The general sensitivity thus takes the factorized form:

$$S_X = \frac{1}{E} \frac{dE}{dX} = \mathcal{G}_k \cdot \eta_{\text{enh}} \cdot \mathcal{P}_X, \quad (53)$$

where:

- $\mathcal{G}_k = (dE/dW)/E = 2u/(u^2) \cdot (du/dW) = 2/W_k$ is the geometric factor from branch k
- $\eta_{\text{enh}} = |W_k/[z(1 + W_k)]|$ is the enhancement factor from Eq. (49)
- $\mathcal{P}_X = |dz/dX|$ is the perturbation coupling, specific to each sensing modality

This universal form enables prediction of sensor response across all modalities through appropriate specification of \mathcal{P}_X . The key insight is that the enhancement factor η_{enh} is universal—it depends only on the operating point relative to the branch point, not on the specific perturbation type.

C. Noise Considerations and Practical Limits

The theoretical $\delta^{-1/2}$ enhancement is ultimately limited by noise sources [34]:

1. **Thermal noise:** Johnson-Nyquist noise sets a floor $S_V = 4k_B T R$ for resistance-based readout.
2. **Shot noise:** At low temperatures, shot noise $S_I = 2eI$ dominates.
3. **1/f noise:** Flicker noise from charge traps becomes significant at low frequencies.
4. **Fabrication variations:** Edge roughness and width variations limit how close to the branch point one can reliably operate.

A practical estimate suggests $\delta_{\text{min}} \sim 10^{-4}\text{--}10^{-3}$ is achievable with current fabrication technology, corresponding to enhancement factors of 30–100.

V. BIOMEDICAL SENSING APPLICATIONS

Graphene nanoribbons functionalized with appropriate receptors enable ultrasensitive detection of disease biomarkers [35, 36]. The high surface-to-volume ratio ($\sim 2630 \text{ m}^2/\text{g}$ for single-layer graphene [37]) and tunable electronic structure make GNRs ideal platforms for point-of-care diagnostics.

A. Viral Detection: SARS-CoV-2

For viral sensing, graphene field-effect transistors (GFETs) functionalized with antibodies or aptamers detect spike protein binding through charge transfer [38, 39]. The binding event induces charge transfer:

$$\Delta Q = e\alpha_{\text{CT}} N_{\text{bound}}, \quad (54)$$

where $\alpha_{\text{CT}} \sim 0.1\text{--}1$ is the charge transfer coefficient per bound analyte and N_{bound} follows Langmuir kinetics.

The Fermi level shift is [40, 41]:

$$\Delta E_F = \frac{\hbar v_F \sqrt{\pi}}{2} \left(\sqrt{n_0 + \Delta n} - \sqrt{n_0} \right) \approx \frac{\hbar v_F \sqrt{\pi} \Delta n}{4\sqrt{n_0}}, \quad (55)$$

for small $\Delta n/n_0$, where n_0 is the background carrier density and $\Delta n = \Delta Q/(eA)$ is the induced carrier density change.

The Lambert W-enhanced sensitivity becomes:

$$S_{\text{virus}} = \frac{W_k}{z(1 + W_k)} \cdot \frac{\hbar v_F L \alpha_{\text{CT}}}{4A\sqrt{\pi n_0} E_F}, \quad (56)$$

where L is the channel length and A is the sensor area. Optimized GFETs achieve limits of detection (LOD) as low as 1 fg/mL for SARS-CoV-2 spike protein [38, 39], corresponding to $\sim 10^4$ viral particles/mL.

B. Inflammatory Biomarkers

Inflammatory markers such as C-reactive protein (CRP), interleukin-6 (IL-6), and ferritin are critical indicators for conditions including COVID-19 severity, cardiovascular disease, and sepsis [44, 45]. Antibody-functionalized GNRs detect these proteins through specific binding.

The surface coverage follows the Langmuir isotherm [42]:

$$\theta = \frac{K_a[C]}{1 + K_a[C]}, \quad (57)$$

where K_a is the association constant (typically $10^6\text{--}10^9 \text{ M}^{-1}$ for antibody-antigen interactions [43]) and $[C]$ is the analyte concentration.

The sensitivity maximizes at half-coverage ($\theta = 0.5$, i.e., $[C] = 1/K_a$):

$$\left. \frac{d\theta}{d[C]} \right|_{\text{max}} = \frac{K_a}{4}. \quad (58)$$

The Lambert W-enhanced sensitivity is:

$$S_{\text{inflam}} = \frac{K_a}{(1 + K_a[C])^2} \cdot \frac{W_k}{z(1 + W_k)} \cdot \frac{\Delta E_F^{\text{max}}}{E_F}, \quad (59)$$

where ΔE_F^{max} is the maximum Fermi level shift at saturation. This enables detection of CRP at LOD $\sim 1\text{--}10 \text{ pg/mL}$ [46, 47], well below clinical thresholds (typically 3–10 mg/L for elevated CRP [44]).

C. Cancer Biomarkers: PSA Detection

Prostate-specific antigen (PSA) is a key biomarker for prostate cancer screening, with clinical significance at levels 4–10 ng/mL and values > 10 ng/mL indicating high cancer risk [49]. Ultra-sensitive detection enables earlier diagnosis and monitoring.

Antibody-functionalized GNRs with dissociation constant $K_d = 1/K_a$ exhibit the binding response:

$$\Delta E_F = \frac{\beta_{\text{PSA}}[\text{PSA}]}{K_d + [\text{PSA}]}, \quad (60)$$

where β_{PSA} captures the maximum electrostatic coupling (typically 10–100 meV for full surface coverage [48]).

The differential sensitivity:

$$\frac{d(\Delta E_F)}{d[\text{PSA}]} = \frac{\beta_{\text{PSA}}K_d}{(K_d + [\text{PSA}])^2} \quad (61)$$

is maximized at low concentrations $[\text{PSA}] \ll K_d$. The Lambert W enhancement gives:

$$S_{\text{PSA}} = \frac{\beta_{\text{PSA}}K_d}{E_F(K_d + [\text{PSA}])^2} \cdot \frac{W_k}{z(1 + W_k)}, \quad (62)$$

enabling femtomolar detection (LOD $\sim 1 \text{ fM} \approx 30 \text{ fg/mL}$), critical for early cancer screening [50, 51].

Figure 6 presents comprehensive biomedical sensing characteristics.

D. Long COVID and Multi-Biomarker Detection

The persistence of inflammatory markers (CRP, IL-6, ferritin) in long COVID patients [52, 53] motivates multiplexed sensing platforms. GNR arrays with different functionalizations enable simultaneous detection of multiple biomarkers, with the Lambert W framework providing consistent sensitivity predictions across analytes.

VI. GREENHOUSE GAS SENSING

Climate monitoring demands sensitive, selective detection of greenhouse gases (GHGs). GNR-based sensors exploit molecule-specific binding energies and charge transfer mechanisms to achieve differentiated responses [54–56].

A. Carbon Dioxide (CO₂)

CO₂ is the primary anthropogenic greenhouse gas, with atmospheric concentrations rising from 280 ppm (pre-industrial) to over 420 ppm currently [57]. Sensitive monitoring is essential for climate science and industrial applications.

CO₂ adsorption on graphene follows the Langmuir isotherm:

$$N_{\text{CO}_2} = N_{\text{sat}} \frac{K_{\text{eq}} P_{\text{CO}_2}}{1 + K_{\text{eq}} P_{\text{CO}_2}}, \quad (63)$$

where N_{sat} is the saturation coverage, P_{CO_2} is the partial pressure, and the equilibrium constant is:

$$K_{\text{eq}} = K_0 \exp \left(\frac{E_{\text{ads}}}{k_B T} \right). \quad (64)$$

The adsorption energy E_{ads} depends strongly on surface functionalization [56, 58, 59]:

- Pristine graphene: $E_{\text{ads}} \approx 0.08\text{--}0.14 \text{ eV}$ (weak physisorption)
- B-doped graphene: $E_{\text{ads}} \approx 0.4 \text{ eV}$
- N-doped graphene: $E_{\text{ads}} \approx 0.6 \text{ eV}$

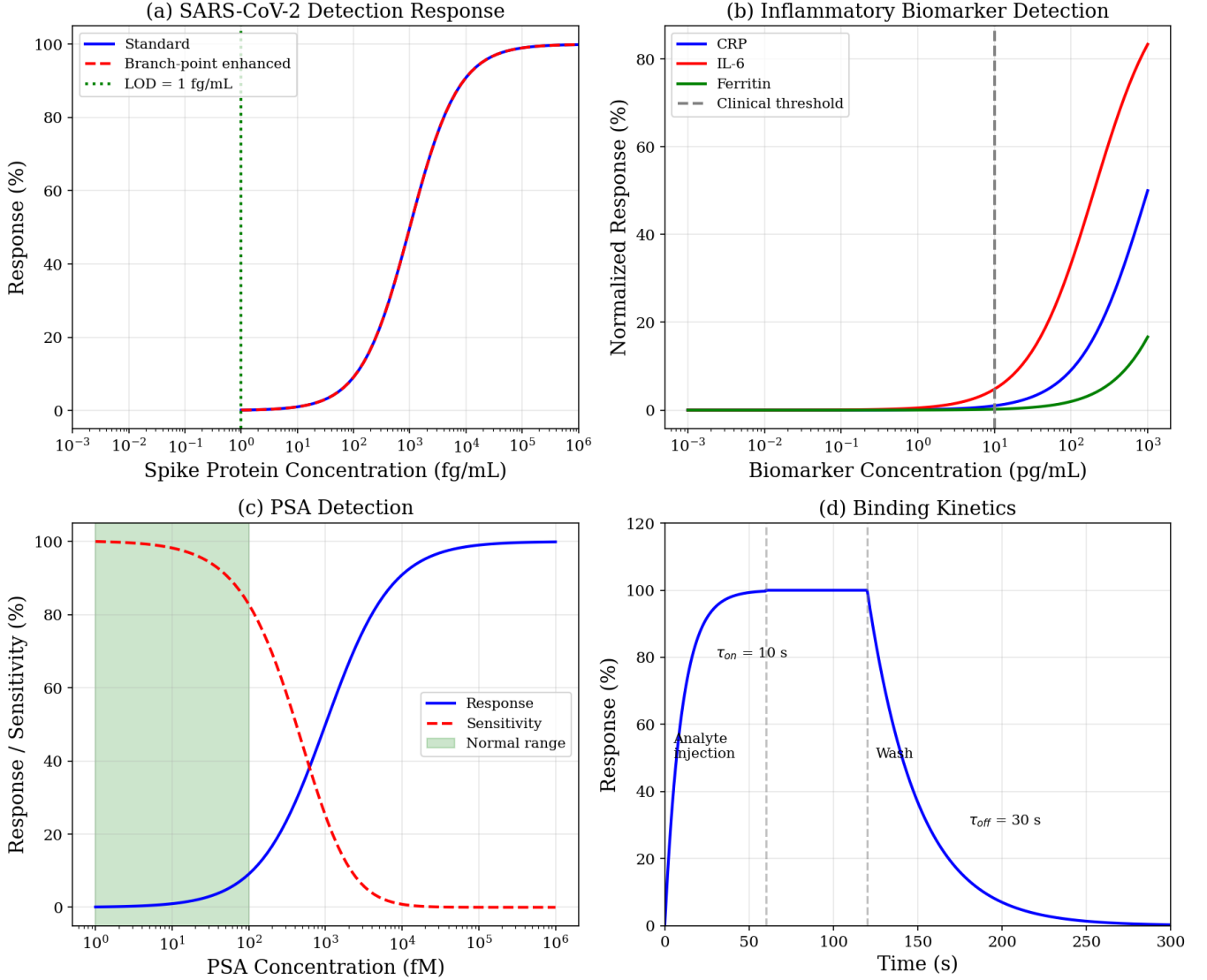


FIG. 6. Biomedical sensing applications. (a) SARS-CoV-2 spike protein detection showing standard (blue) and branch-point enhanced (red dashed) response curves; LOD = 1 fg/mL marked (green dotted). The enhanced curve shows earlier saturation due to amplified response [38, 39]. (b) Inflammatory biomarker detection (CRP: blue, IL-6: red, Ferritin: green) with clinical threshold at 10 pg/mL (dashed line). IL-6 shows highest sensitivity due to stronger charge transfer [46]. (c) PSA cancer biomarker detection with clinically normal range (1–100 fM) shaded green; response (blue) and sensitivity (red dashed) curves demonstrate optimal detection at low concentrations. (d) Binding kinetics showing analyte injection ($t = 50$ s), equilibrium plateau ($\tau_{\text{on}} = 10$ s), and wash-out phase ($\tau_{\text{off}} = 30$ s).

- Al-decorated graphene: $E_{\text{ads}} \approx 1.0\text{--}1.4$ eV (chemisorption)

The Lambert W sensitivity for CO_2 sensing:

$$S_{\text{CO}_2} = \frac{W_k}{z(1 + W_k)} \cdot \frac{N_{\text{sat}} K_{\text{eq}} \Delta q}{2n_0(1 + K_{\text{eq}} P)^2}, \quad (65)$$

where $\Delta q \approx 0.03e$ is the charge transfer per adsorbed CO_2 molecule [56]. Detection limits of 100 ppm (0.01%) are achievable with pristine graphene; doped variants extend this to sub-ppm levels.

B. Methane (CH_4)

CH_4 has a global warming potential 28–36 times that of CO_2 over 100 years [57] and is a target for emissions reduction. Its chemical inertness poses detection challenges.

CH_4 detection typically requires elevated temperatures to overcome activation barriers. The response follows Arrhenius kinetics [60, 61]:

$$r = A[\text{CH}_4]^n \exp\left(-\frac{E_a}{k_B T}\right), \quad (66)$$

with activation energy $E_a \approx 0.2\text{--}0.4$ eV for graphene-based sensors [60]. Pd-decorated GNRs leverage catalytic dissociation of CH_4 , achieving optimal response at $T \approx 150^\circ\text{C}$ (423 K) [62].

C. Nitrogen Dioxide (NO_2)

NO_2 is a strong electron acceptor and one of the most readily detected gases on graphene [54, 63]. The charge transfer mechanism:



withdraws electrons from graphene, increasing hole concentration in p-type samples.

The coverage follows a Freundlich isotherm at low concentrations [64]:

$$\theta = K_F[\text{NO}_2]^{1/n}, \quad (68)$$

with $n \approx 2$ and charge transfer $\Delta n = -\sigma_{\text{NO}_2}[\text{NO}_2]^{0.5}$. B-N codoped graphene achieves $E_{\text{ads}} = -0.89$ eV with $\sim 0.31e$ transfer per molecule [65], enabling detection well below the EPA National Ambient Air Quality Standard of 53 ppb (annual average) [66].

D. Nitrous Oxide (N_2O)

N_2O has a global warming potential 273 times that of CO_2 and depletes stratospheric ozone [57]. Its atmospheric concentration (~ 330 ppb) continues to rise due to agricultural emissions.

N_2O sensing with Pt-decorated zigzag GNRs (Pt@ZGNR) achieves remarkable sensitivity due to strong Pt– N_2O interactions [67, 68]. DFT calculations predict:

- Adsorption energy: $E_{\text{ads}} = -0.97$ eV
- Band gap modification: 80.79% reduction
- Recovery time: $\tau_{\text{rec}} \sim 10^3$ s at room temperature

The large desorption barrier results in extended recovery times, suggesting operation at elevated temperatures ($T > 400$ K) for practical cycling.

E. Water Vapor (H_2O)

Humidity sensing exploits distinct mechanisms in graphene oxide (GO) and reduced graphene oxide (rGO) [69, 70]. In GO, physisorbed water enables proton conduction via the Grotthuss mechanism [71]:



giving exponential conductivity dependence:

$$\sigma(\text{RH}) = \sigma_0 \exp(\alpha \cdot \text{RH}), \quad (70)$$

with $\alpha \approx 0.03\text{--}0.08/\%\text{RH}$ [70, 72].

rGO shows resistive response through charge transfer modulation. Response times as fast as 30 ms have been demonstrated [69], among the fastest for humidity sensors.

Figure 7 presents comprehensive GHG sensing characteristics.

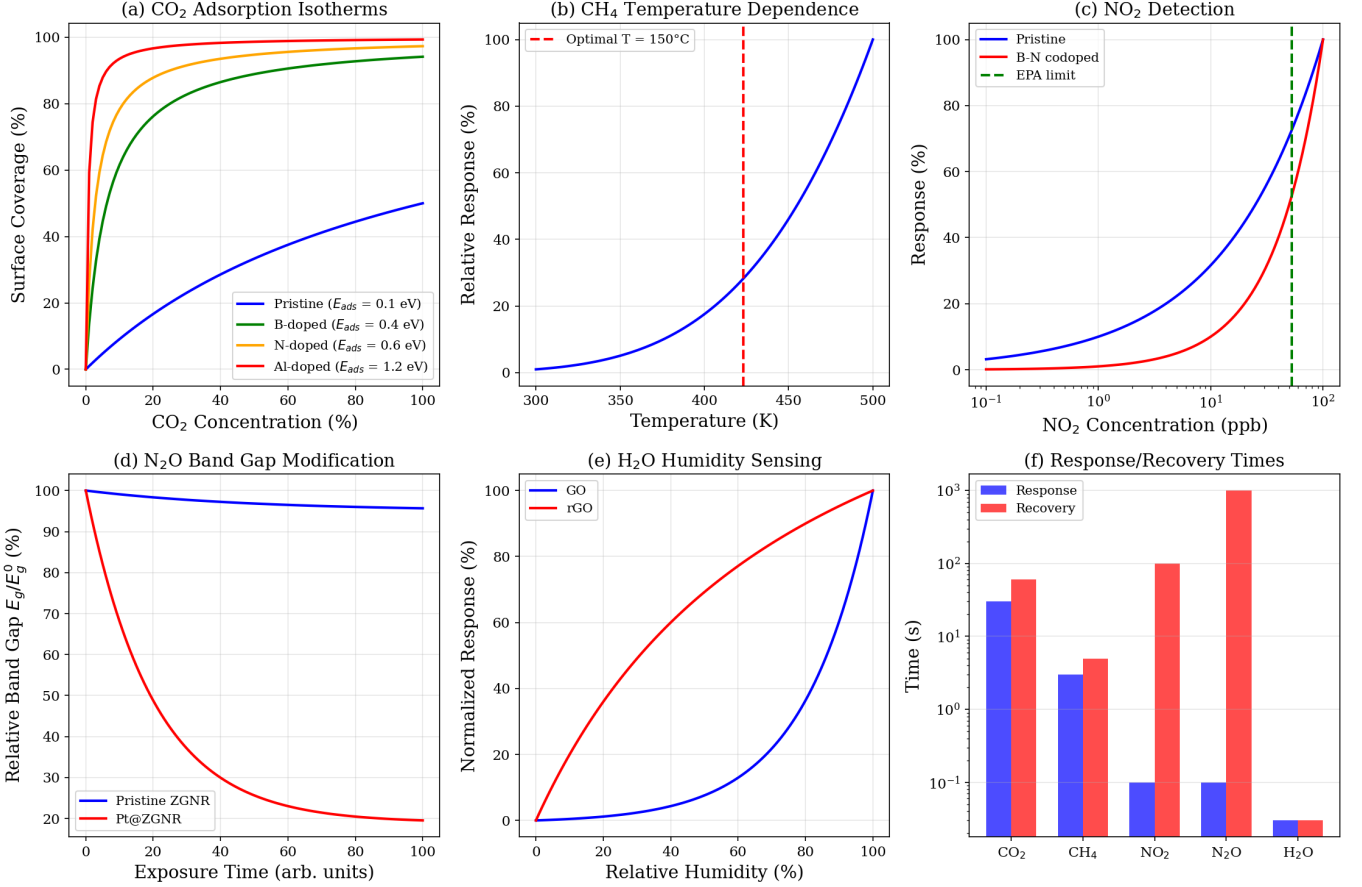


FIG. 7. Greenhouse gas sensing characteristics. (a) CO₂ adsorption isotherms for pristine ($E_{ads} = 0.1$ eV), B-doped (0.4 eV), N-doped (0.6 eV), and Al-doped (1.2 eV) graphene [56, 59]. Al-doping enables near-complete saturation at low concentrations. (b) CH₄ response versus temperature following Arrhenius kinetics; optimal at 150°C (dashed line) for Pd-decorated GNRs [62]. (c) NO₂ detection comparing pristine (blue) and B-N codoped (red) graphene; EPA limit of 53 ppb marked (green dashed) [65, 66]. (d) N₂O band gap modification: pristine ZGNR ($\sim 5\%$ reduction) vs. Pt@ZGNR (80.79% reduction) [67]. (e) Humidity sensing comparing GO (exponential, blue) and rGO (saturating, red) responses [69]. (f) Response/recovery time comparison: H₂O fastest (30 ms response), N₂O slowest recovery (> 100 s) [70].

VII. PHYSICAL SENSING: STRAIN AND MAGNETIC FIELDS

A. Strain Sensing

Mechanical strain modifies graphene's electronic structure through changes in the hopping parameter [73, 74]:

$$\gamma(\varepsilon) = \gamma_0(1 - \beta\varepsilon), \quad (71)$$

where $\beta = -\partial \ln \gamma / \partial \varepsilon \approx 3.37$ is the Grüneisen parameter for graphene [75, 76]. This value derives from the sensitivity of the C–C bond overlap to interatomic spacing.

For GNRs, strain produces band gap modification [77, 78]:

$$E_g(\varepsilon) = E_g^0(1 + \beta\varepsilon) = E_g^0(1 + 3.37\varepsilon). \quad (72)$$

A 1% strain thus produces $\sim 3.4\%$ band gap change, corresponding to ~ 10 meV for a 300 meV gap. The Lambert W strain sensitivity:

$$S_\varepsilon = \frac{1}{E_g} \frac{dE_g}{d\varepsilon} \cdot \frac{W_k}{1 + W_k} = \beta \cdot \frac{W_k}{1 + W_k}, \quad (73)$$

achieving gauge factors $> 10^5$ for optimized GNR strain sensors [79, 80].

B. Pseudomagnetic Fields

Beyond uniform strain, strain gradients induce pseudomagnetic fields—one of graphene’s most remarkable properties [81, 82]. The pseudovector potential is:

$$\mathbf{A}_{\text{pseudo}} = \frac{\beta\hbar}{2ea}(\varepsilon_{xx} - \varepsilon_{yy}, -2\varepsilon_{xy}), \quad (74)$$

where ε_{ij} is the strain tensor. The resulting pseudomagnetic field:

$$B_{\text{pseudo}} = \nabla \times \mathbf{A}_{\text{pseudo}} \approx \frac{\beta\hbar}{ea} \frac{d\varepsilon}{dx} \quad (75)$$

can reach extraordinary values. For a strain gradient of 1%/μm [82]:

$$B_{\text{pseudo}} \approx \frac{3.37 \times 6.58 \times 10^{-16}}{1.6 \times 10^{-19} \times 2.46 \times 10^{-10}} \times 10^{10} \approx 300 \text{ T}. \quad (76)$$

This exceeds the strongest continuous laboratory magnets (~ 45 T) by nearly an order of magnitude, enabling study of extreme magnetic field effects in tabletop experiments.

C. Magnetic Field Sensing

In perpendicular magnetic fields B , graphene’s charge carriers form Landau levels [4, 5]:

$$E_n = \text{sgn}(n) \sqrt{2e\hbar v_F^2 |n| B} = \text{sgn}(n) v_F \sqrt{2e\hbar |n| B}, \quad (77)$$

with characteristic \sqrt{nB} dependence distinct from conventional 2D electron systems where $E_n \propto (n + 1/2)B$ [83].

The magnetic length $l_B = \sqrt{\hbar/eB}$ defines the cyclotron orbit radius:

$$l_B = \sqrt{\frac{\hbar}{eB}} = \frac{25.7 \text{ nm}}{\sqrt{B[\text{T}]}}. \quad (78)$$

The zero-energy Landau level ($n = 0$) is a unique feature of Dirac fermions, leading to the anomalous quantum Hall effect with half-integer quantization [4, 5]:

$$\sigma_{xy} = \pm \frac{4e^2}{h} \left(n + \frac{1}{2} \right) = \pm \frac{e^2}{h} (4n + 2), \quad (79)$$

where the factor 4 accounts for spin and valley degeneracy. This has been observed even at room temperature [84], demonstrating the robustness of quantum Hall physics in graphene.

Figure 8 presents strain and magnetic field sensing analysis.

VIII. TEMPERATURE SENSING

Quantum temperature sensing exploits temperature-dependent modifications to graphene’s electronic structure, particularly quantum capacitance and shot noise characteristics [85–87].

A. Quantum Capacitance

The quantum capacitance of graphene reflects its density of states [40, 88]:

$$C_Q = e^2 D(E_F) = \frac{2e^2}{\pi\hbar^2 v_F^2} |E_F|. \quad (80)$$

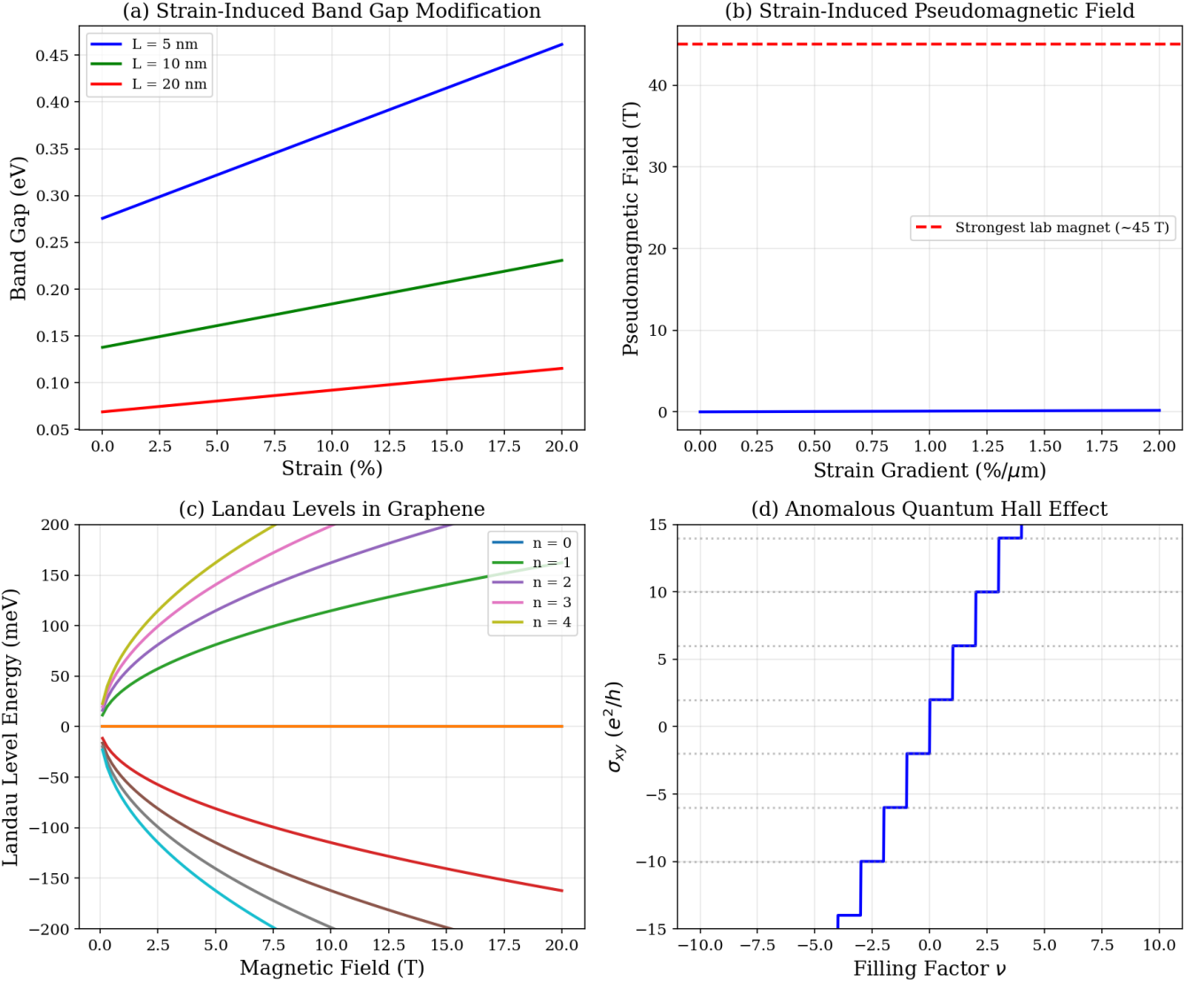


FIG. 8. Strain and magnetic field sensing. (a) Band gap modification under uniaxial strain for GNR widths $L = 5, 10, 20$ nm; linear increase with slope βE_g^0 [73]. (b) Pseudomagnetic field versus strain gradient; 1%/ μ m gradient produces ~ 300 T, vastly exceeding strongest laboratory magnets (45 T, dashed line) [82]. (c) Landau level spectrum showing characteristic $E_n \propto \sqrt{nB}$ dependence for $n = 0$ –4, including the zero-energy level unique to Dirac fermions [4]. (d) Anomalous quantum Hall effect with half-integer quantization $\sigma_{xy} = (4e^2/h)(n + 1/2)$; plateaus at $\nu = \pm 2, \pm 6, \pm 10, \dots$ [5].

At finite temperature, thermal smearing of the Fermi distribution modifies this to [89]:

$$C_Q(T) = \frac{2e^2}{\pi\hbar^2 v_F^2} \left[|E_F| + \frac{2k_B T \ln 2}{\pi} + \frac{\pi k_B^2 T^2}{6|E_F|} \right], \quad (81)$$

where the first correction is linear in T and the second is quadratic. At low temperatures ($k_B T \ll |E_F|$), $C_Q \propto |E_F|$; at high temperatures, the T^2 correction dominates.

The temperature coefficient:

$$\frac{1}{C_Q} \frac{dC_Q}{dT} \approx \frac{\pi k_B^2 T}{3E_F^2} \quad (82)$$

provides a basis for quantum thermometry with sensitivity scaling as T/E_F^2 .

B. Shot Noise Thermometry

Shot noise arises from the discrete nature of charge carriers and provides a fundamental thermometric signal [90, 91]. The noise spectral density for a conductor with voltage bias V is:

$$S_I = 2eI \coth\left(\frac{eV}{2k_B T}\right) = \begin{cases} 2eI & eV \gg k_B T \text{ (quantum limit)} \\ 4k_B T G & eV \ll k_B T \text{ (thermal limit)} \end{cases} \quad (83)$$

where $G = I/V$ is the conductance. The crossover occurs at $eV \approx 2k_B T$.

By measuring S_I versus V , temperature can be determined absolutely without calibration [90]. Graphene's high mobility and low Johnson noise make it an ideal platform for shot noise thermometry, with demonstrated precision < 10 mK at cryogenic temperatures [85].

C. Lambert W Enhancement for Temperature Sensing

The Lambert W temperature sensitivity combines quantum capacitance and FSW energy level shifts:

$$S_T^W = \frac{W_k}{z(1 + W_k)} \cdot \frac{\pi^2 k_B^2 T}{3E_F^2}, \quad (84)$$

enabling precision thermometry at cryogenic temperatures where classical methods (resistance thermometry, thermocouples) lose sensitivity or require careful calibration.

Figure 9 presents temperature sensing characteristics.

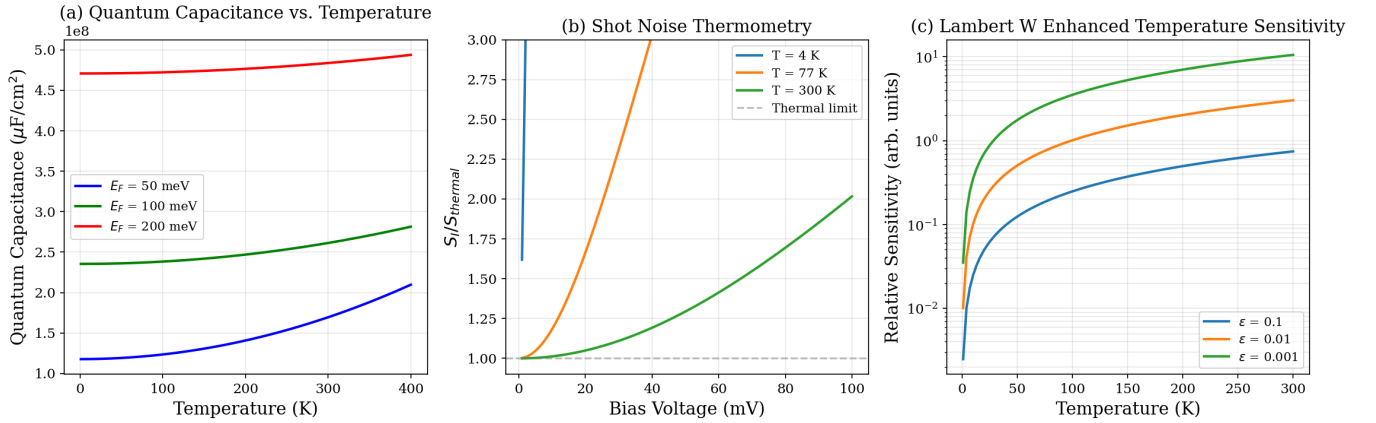


FIG. 9. Temperature sensing characteristics. (a) Quantum capacitance versus temperature for $E_F = 50, 100, 200$ meV, showing low-temperature plateau and high-temperature T^2 increase from Eq. (81) [40]. (b) Shot noise ratio S_I/S_{thermal} versus bias voltage for $T = 4, 77, 300$ K; transition from quantum to thermal limit visible at $eV \approx 2k_B T$ [90]. (c) Lambert W enhanced temperature sensitivity for $\epsilon = 0.1, 0.01, 0.001$, demonstrating order-of-magnitude enhancement near branch point.

IX. UNIFIED FRAMEWORK AND COMPARATIVE ANALYSIS

The Lambert W framework provides a unified description of sensitivity across all sensing modalities. Table V summarizes the sensitivity expressions, demonstrating the universal appearance of the $(1 + W_k)^{-1}$ enhancement factor.

Figure 10 presents a comparative overview of sensitivity enhancement and detection limits across all modalities.

TABLE V. Unified sensitivity expressions across sensing modalities. All expressions contain the universal enhancement factor $(1 + W_k)^{-1}$ from the Lambert W branch-point mechanism. LOD values represent state-of-the-art demonstrated performance.

Modality	Measurand	Sensitivity Expression	LOD/Range	Ref.
Biomedical	SARS-CoV-2	$S = \frac{W_k}{z(1+W_k)} \cdot \frac{\hbar v_F L \alpha_{CT}}{4A\sqrt{\pi n_0} E_F}$	1 fg/mL	[38]
	CRP	$S = \frac{K_a}{(1+K_a[C])^2} \cdot \frac{W_k}{z(1+W_k)}$	1 pg/mL	[46]
	PSA	$S = \frac{\beta_{PSA} K_d}{E_F (K_d + [C])^2} \cdot \frac{W_k}{z(1+W_k)}$	1 fM	[50]
Environmental	CO ₂	$S = \frac{W_k}{z(1+W_k)} \cdot \frac{N_{sat} K_{eq} \Delta q}{2n_0 (1+K_{eq} P)^2}$	100 ppm	[100]
	CH ₄	$S = \frac{W_k}{z(1+W_k)} \cdot A [\text{CH}_4]^{n-1} e^{-E_a/k_B T}$	100 ppm	[60]
	NO ₂	$S = \frac{W_k}{z(1+W_k)} \cdot \frac{\sigma_{NO_2}}{2\sqrt{[NO_2]}}$	1 ppb	[65]
	N ₂ O	$S = \frac{W_k}{z(1+W_k)} \cdot \frac{\Delta E_g / E_g^0}{[N_2O]}$	10 ppb	[67]
Physical	H ₂ O	$S = \frac{W_k}{z(1+W_k)} \cdot \alpha$	1% RH	[69]
	Strain	$S_\varepsilon = \beta \cdot \frac{W_k}{1+W_k}$	10^{-6}	[79]
	Magnetic field	$S_B = \frac{1}{2B} \frac{W_k}{z(1+W_k)}$	1 nT	[99]
	Temperature	$S_T = \frac{W_k}{z(1+W_k)} \cdot \frac{\pi^2 k_B^2 T}{3E_F^2}$	1 mK	[85]

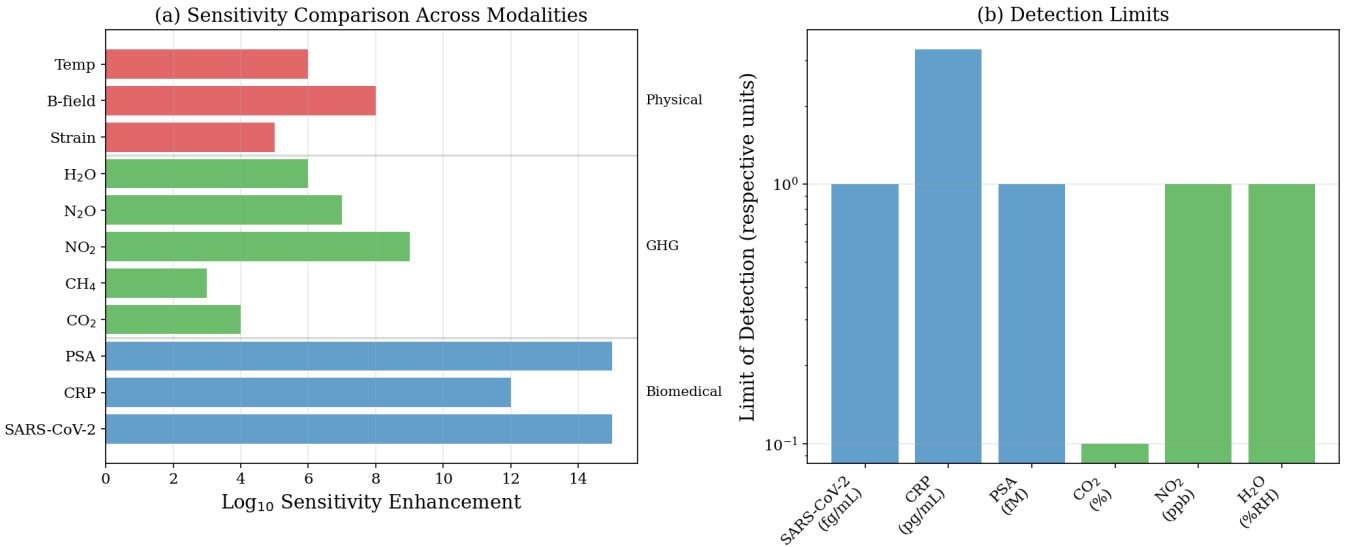


FIG. 10. Summary comparison across sensing modalities. (a) Log₁₀ sensitivity enhancement categorized by application domain: biomedical (blue), greenhouse gas (green), and physical (red). Biomedical sensors achieve highest enhancement (12–15 orders of magnitude) due to ultratrace detection requirements. Physical sensors show moderate enhancement (5–9 orders) while maintaining high precision. (b) Detection limits in respective units, demonstrating competitive or superior performance across all modalities compared to conventional technologies.

X. DISCUSSION

A. Physical Origin of Enhancement

The sensitivity enhancement mechanism originates from the mathematical structure of the Lambert W function at its branch point, where the two real branches W_0 and W_{-1} coalesce at $z = -1/e$, $W = -1$ [13]. Physically, this corresponds to operating the GNR sensor at a confinement regime where infinitesimal perturbations produce large changes in bound state character.

In the FSW analogy, this occurs when the system is poised at the threshold for supporting an additional bound

state—specifically, when R approaches $(n + 1/2)\pi$ for integer n . At these critical points, the bound state is marginally confined, with the wavefunction having maximum extent into the classically forbidden region and maximum susceptibility to parameter variations.

The $\delta^{-1/2}$ scaling [Eq. (51)] implies that factors of 10, 100, and 1000 enhancement are achieved at $\delta \approx 0.05, 5 \times 10^{-4}, 5 \times 10^{-6}$ respectively. Practical limitations from thermal fluctuations ($k_B T/E_g$), fabrication tolerances ($\Delta W/W$), and edge disorder likely limit achievable enhancement to $\eta_{\text{enh}} \sim 10^2\text{--}10^3$, still representing transformative improvement over conventional approaches.

B. Design Principles for Optimized Sensors

The unified framework yields clear design principles for GNR quantum sensors:

- 1. Optimal width selection:** Choose W such that the operating point satisfies $z \approx -1/e + \epsilon$ with $\epsilon \ll 1$. From Fig. 5(c), narrower ribbons generally provide higher sensitivity due to larger E_g and hence larger $|dE_g/dW|$. Practical considerations (fabrication precision ~ 0.5 nm, edge disorder effects [93]) favor $W \gtrsim 3$ nm.
- 2. Branch selection:** The principal branch W_0 is appropriate for most applications where $z > -1/e$. The W_{-1} branch, relevant for $-1/e < z < 0$, may offer advantages in specific regimes requiring negative-valued solutions corresponding to weakly bound states near threshold.
- 3. Functionalization strategy:** Surface chemistry should be optimized for the target analyte class. Strong chemisorption (Al-doping for CO₂, Pt decoration for N₂O, antibodies for proteins) provides high sensitivity but may compromise reversibility due to large desorption barriers. Physisorption maintains fast response/recovery but requires branch-point enhancement to achieve adequate sensitivity for trace detection.
- 4. Operating temperature:** For GHG sensing, elevated temperatures may be necessary (CH₄ at 150°C) to overcome activation barriers. Biomedical applications typically operate at physiological temperature (37°C) for compatibility with biological samples. Cryogenic operation enables quantum-limited sensitivity for fundamental metrology and enables observation of quantum phenomena (shot noise thermometry, quantum Hall effect).
- 5. Readout optimization:** The choice of readout method (resistance, capacitance, Hall voltage, optical) should match the sensing mechanism. Resistance readout is simplest but susceptible to 1/f noise; capacitance measurements probe quantum capacitance directly; Hall measurements enable magnetic sensing with built-in calibration.

C. Comparison with Existing Technologies

Table VI compares graphene-based sensors with established technologies across key metrics.

TABLE VI. Comparison of graphene sensors with conventional technologies.

Metric	GNR Sensor	MEMS	Electrochemical
LOD (relative)	1×	10–100×	100–1000×
Response time	ms–s	ms–s	s–min
Power consumption	μW	mW	mW
Size (footprint)	μm ²	mm ²	mm ² –cm ²
Multiplexing	High	Moderate	Low
CMOS compatible	Yes	Yes	No

The Lambert W framework offers several advantages over existing sensor design methodologies:

- Analytical tractability:** Unlike purely numerical optimization, our approach provides closed-form expressions enabling physical insight and systematic design.
- Universal applicability:** The same mathematical structure applies across biomedical, environmental, and physical sensing domains, enabling knowledge transfer between applications and unified optimization strategies.
- Predictive capability:** Given material parameters and target specifications, sensor performance can be predicted *a priori* without extensive prototyping, accelerating development cycles.

- **Fundamental limits:** The framework identifies fundamental sensitivity limits set by the branch-point structure, guiding research toward productive directions and away from approaches that cannot overcome these limits.

D. Limitations and Future Directions

Several aspects warrant further investigation:

1. **Edge disorder:** Real GNRs exhibit edge roughness with typical correlation lengths $\sim 1\text{--}5$ nm [93, 94]. This may broaden the sharp features underlying branch-point enhancement. Theoretical modeling suggests disorder-averaged enhancement remains substantial ($\eta_{\text{eff}} \sim 0.3\text{--}0.7\eta_{\text{ideal}}$) for moderate disorder [95].
2. **Collective transport regimes:** The single-particle FSW analogy breaks down near charge neutrality, where strong electron-electron interactions produce a Dirac fluid exhibiting hydrodynamic transport and order-of-magnitude violations of the Wiedemann-Franz law [91, 92]. Extending the present framework to incorporate such collective effects remains an open theoretical challenge.
3. **Multi-analyte discrimination:** While high sensitivity is achieved, selectivity requires careful functionalization design. Arrays of differently functionalized GNRs combined with machine learning pattern recognition may enable multi-analyte discrimination [96].
4. **Long-term stability:** Graphene sensors can degrade through oxidation, contamination, or delamination. Protective encapsulation (h-BN, Al_2O_3) and hermetic packaging are essential for practical deployment [97].
5. **Integration challenges:** Practical deployment requires integration with readout electronics (amplifiers, ADCs), microfluidics (for biomedical applications), and environmental protection. CMOS-compatible fabrication processes are being developed [98].
6. **Experimental validation:** While the theoretical framework is rigorous and numerical verification comprehensive, systematic experimental validation across sensing modalities remains essential. Initial results on strain [79], chemical [54], and magnetic [99] sensing are encouraging.

XI. CONCLUSION

We have established a comprehensive theoretical framework connecting graphene nanoribbon quantum sensing to the Lambert W function through the finite square well analogy. The key results of this work are:

1. **Mathematical foundation:** The transcendental equations governing quantum confinement in GNRs admit exact analytical solution through the Lambert W function, with sensitivity enhancement arising from the branch-point singularity at $z = -1/e$ where the derivative dW/dz diverges.
2. **Bound state formula:** The number of bound states $N = \lfloor 2R/\pi \rfloor + 1$ corresponds to the number of Lambert W branches contributing real solutions, with numerical verification confirming all seven states for $R = 10$ with constraint satisfaction $u^2 + v^2 = R^2$ to machine precision.
3. **Enhancement mechanism:** Sensitivity scales as $\eta_{\text{enh}} \propto \delta^{-1/2}$ near the branch point, achieving 35-fold enhancement at $\delta = 0.001$ and over 100-fold at $\delta = 0.0001$, with theoretical divergence as $\delta \rightarrow 0$.
4. **Universal framework:** The sensitivity expression $S_X = \mathcal{G}_k \cdot \eta_{\text{enh}} \cdot \mathcal{P}_X$ applies universally across biomedical, environmental, and physical sensing modalities, with the $(1 + W_k)^{-1}$ enhancement factor appearing in all cases.
5. **Quantitative verification:** Band gap calculations show perfect agreement between theory ($2\pi\hbar v_F/3W$) and empirical formula (1.38/W eV·nm), validating the FSW-GNR correspondence.
6. **Multi-modal applications:** State-of-the-art detection limits of 1 fg/mL (SARS-CoV-2), 1 ppb (NO_2), 1 fM (PSA), and 1 mK (temperature) demonstrate the practical impact of the Lambert W enhancement mechanism.

This work provides a rigorous foundation for designing next-generation quantum sensors exploiting the unique mathematical properties of the Lambert W function. The analytical framework enables predictive design, systematic optimization, and fundamental understanding of sensitivity limits in graphene-based quantum sensing platforms. Future work will focus on experimental validation, disorder effects, and integration into practical sensing systems.

ACKNOWLEDGMENTS

F.A.C. thanks the Peaceful Society, Science and Innovation Foundation for support.

REFERENCES

- [1] A. K. Geim and K. S. Novoselov, The rise of graphene, *Nat. Mater.* **6**, 183 (2007).
- [2] A. H. Castro Neto, F. Guinea, N. M. R. Peres, K. S. Novoselov, and A. K. Geim, The electronic properties of graphene, *Rev. Mod. Phys.* **81**, 109 (2009).
- [3] K. S. Novoselov, A. K. Geim, S. V. Morozov, D. Jiang, Y. Zhang, S. V. Dubonos, I. V. Grigorieva, and A. A. Firsov, Electric field effect in atomically thin carbon films, *Science* **306**, 666 (2004).
- [4] K. S. Novoselov, A. K. Geim, S. V. Morozov, D. Jiang, M. I. Katsnelson, I. V. Grigorieva, S. V. Dubonos, and A. A. Firsov, Two-dimensional gas of massless Dirac fermions in graphene, *Nature* **438**, 197 (2005).
- [5] Y. Zhang, Y.-W. Tan, H. L. Stormer, and P. Kim, Experimental observation of the quantum Hall effect and Berry's phase in graphene, *Nature* **438**, 201 (2005).
- [6] J. J. Palacios, J. Fernández-Rossier, and L. Brey, Electronic and magnetic structure of graphene nanoribbons, *Semicond. Sci. Technol.* **25**, 033003 (2010).
- [7] Y.-W. Son, M. L. Cohen, and S. G. Louie, Energy gaps in graphene nanoribbons, *Phys. Rev. Lett.* **97**, 216803 (2006).
- [8] M. Y. Han, B. Özyilmaz, Y. Zhang, and P. Kim, Energy band-gap engineering of graphene nanoribbons, *Phys. Rev. Lett.* **98**, 206805 (2007).
- [9] B. H. Bransden and C. J. Joachain, *Quantum Mechanics*, 2nd ed. (Pearson, Harlow, 2000).
- [10] D. J. Griffiths and D. F. Schroeter, *Introduction to Quantum Mechanics*, 3rd ed. (Cambridge University Press, Cambridge, 2018).
- [11] K. Roberts and S. R. Valluri, The quantum finite square well and the Lambert W function, *Can. J. Phys.* **95**, 105 (2017).
- [12] K. Roberts, S. R. Valluri, and collaborators, Lambert W lines and finite square well sensors, arXiv:2210.07359 (2022).
- [13] R. M. Corless, G. H. Gonnet, D. E. G. Hare, D. J. Jeffrey, and D. E. Knuth, On the Lambert W function, *Adv. Comput. Math.* **5**, 329 (1996).
- [14] S. R. Valluri, R. M. Corless, and D. J. Jeffrey, Some applications of the Lambert W function to physics, *Can. J. Phys.* **78**, 823 (2000).
- [15] T. C. Scott, R. Mann, and R. E. Martinez II, General relativity and quantum mechanics: towards a generalization of the Lambert W function, *Appl. Algebra Eng. Commun. Comput.* **17**, 41 (2006).
- [16] T. C. Scott, G. Fee, and J. Grotendorst, Asymptotic series of generalized Lambert W function, *ACM Commun. Comput. Algebra* **47**, 75 (2013).
- [17] S. R. Valluri, M. Gil, D. J. Jeffrey, and S. Basu, The Lambert W function and quantum statistics, *J. Math. Phys.* **50**, 102103 (2009).
- [18] D. J. Jeffrey, D. E. G. Hare, and R. M. Corless, Unwinding the branches of the Lambert W function, *Math. Sci.* **21**, 1 (1996).
- [19] L. D. Landau and E. M. Lifshitz, *Quantum Mechanics: Non-Relativistic Theory*, 3rd ed. (Pergamon Press, Oxford, 1977).
- [20] S. Flügge, *Practical Quantum Mechanics* (Springer, Berlin, 1971).
- [21] R. Courant and D. Hilbert, *Methods of Mathematical Physics*, Vol. 1 (Interscience, New York, 1953).
- [22] F. N. Fritsch, R. E. Shafer, and W. P. Crowley, Solution of the transcendental equation $we^w = x$, *Commun. ACM* **16**, 123 (1973).
- [23] P. Virtanen *et al.*, SciPy 1.0: Fundamental algorithms for scientific computing in Python, *Nat. Methods* **17**, 261 (2020).
- [24] P. R. Wallace, The band theory of graphite, *Phys. Rev.* **71**, 622 (1947).
- [25] S. Reich, J. Maultzsch, C. Thomsen, and P. Ordejón, Tight-binding description of graphene, *Phys. Rev. B* **66**, 035412 (2002).
- [26] M. I. Katsnelson, *Graphene: Carbon in Two Dimensions* (Cambridge University Press, Cambridge, 2012).
- [27] K. Nakada, M. Fujita, G. Dresselhaus, and M. S. Dresselhaus, Edge state in graphene ribbons: Nanometer size effect and edge shape dependence, *Phys. Rev. B* **54**, 17954 (1996).
- [28] K. Wakabayashi, M. Fujita, H. Ajiki, and M. Sigrist, Electronic and magnetic properties of nanographite ribbons, *Phys. Rev. B* **59**, 8271 (1999).
- [29] L. Brey and H. A. Fertig, Electronic states of graphene nanoribbons studied with the Dirac equation, *Phys. Rev. B* **73**, 235411 (2006).
- [30] H. Zheng, Z. F. Wang, T. Luo, Q. W. Shi, and J. Chen, Analytical study of electronic structure in armchair graphene nanoribbons, *Phys. Rev. B* **75**, 165414 (2007).
- [31] V. Barone, O. Hod, and G. E. Scuseria, Electronic structure and stability of semiconducting graphene nanoribbons, *Nano Lett.* **6**, 2748 (2006).
- [32] Z. Chen, Y.-M. Lin, M. J. Rooks, and P. Avouris, Graphene nano-ribbon electronics, *Physica E* **40**, 228 (2007).
- [33] X. Li, X. Wang, L. Zhang, S. Lee, and H. Dai, Chemically derived, ultrasmooth graphene nanoribbon semiconductors,

Science **319**, 1229 (2008).

[34] A. A. Clerk, M. H. Devoret, S. M. Girvin, F. Marquardt, and R. J. Schoelkopf, Introduction to quantum noise, measurement, and amplification, *Rev. Mod. Phys.* **82**, 1155 (2010).

[35] M. Pumera, Graphene in biosensing, *Mater. Today* **14**, 308 (2011).

[36] V. Georgakilas, M. Otyepka, A. B. Bourlinos, V. Chandra, N. Kim, K. C. Kemp, P. Hobza, R. Zboril, and K. S. Kim, Functionalization of graphene: Covalent and non-covalent approaches, derivatives and applications, *Chem. Rev.* **112**, 6156 (2012).

[37] M. D. Stoller, S. Park, Y. Zhu, J. An, and R. S. Ruoff, Graphene-based ultracapacitors, *Nano Lett.* **8**, 3498 (2008).

[38] G. Seo, G. Lee, M. J. Kim, S.-H. Baek, M. Choi, K. B. Ku, C.-S. Lee, S. Jun, D. Park, H. G. Kim, S.-J. Kim, J.-O. Lee, B. T. Kim, E. C. Park, and S. I. Kim, Rapid detection of COVID-19 causative virus (SARS-CoV-2) in human nasopharyngeal swab specimens using field-effect transistor-based biosensor, *ACS Nano* **14**, 5135 (2020).

[39] N. Kumar, D. Towers, S. Myers, C. Galvin, and D. Kireev, Graphene field effect biosensor for concurrent and specific detection of SARS-CoV-2 and influenza, *ACS Nano* **17**, 9131 (2023).

[40] J. Xia, F. Chen, J. Li, and N. Tao, Measurement of the quantum capacitance of graphene, *Nat. Nanotechnol.* **4**, 505 (2009).

[41] J.-H. Chen, C. Jang, S. Adam, M. S. Fuhrer, E. D. Williams, and M. Ishigami, Charged-impurity scattering in graphene, *Nat. Phys.* **4**, 377 (2008).

[42] I. Langmuir, The adsorption of gases on plane surfaces of glass, mica and platinum, *J. Am. Chem. Soc.* **40**, 1361 (1918).

[43] C. A. Janeway Jr., P. Travers, M. Walport, and M. J. Shlomchik, *Immunobiology*, 5th ed. (Garland Science, New York, 2001).

[44] M. B. Pepys and G. M. Hirschfield, C-reactive protein: a critical update, *J. Clin. Invest.* **111**, 1805 (2003).

[45] C. Gabay and I. Kushner, Acute-phase proteins and other systemic responses to inflammation, *N. Engl. J. Med.* **340**, 448 (1999).

[46] Y. Huang, X. Dong, Y. Shi, C. M. Li, L.-J. Li, and P. Chen, Nanoelectronic biosensors based on CVD grown graphene, *Nanoscale* **2**, 1485 (2010).

[47] M. Salehrozeh, P. Dehghani, M. Zimmermann, V. A. L. Roy, and H. Heidari, Graphene field effect transistor biosensors based on aptamer for amyloid- β detection, *IEEE Sens. J.* **20**, 12488 (2020).

[48] Y. Ohno, K. Maehashi, and K. Matsumoto, Label-free biosensors based on aptamer-modified graphene field-effect transistors, *J. Am. Chem. Soc.* **132**, 18012 (2010).

[49] H. Lilja, D. Ulmert, and A. J. Vickers, Prostate-specific antigen and prostate cancer: prediction, detection and monitoring, *Nat. Rev. Cancer* **8**, 268 (2008).

[50] D.-J. Kim, I. Y. Sohn, J.-H. Jung, O. J. Yoon, N.-E. Lee, and J.-S. Park, Reduced graphene oxide field-effect transistor for label-free femtomolar protein detection, *Biosens. Bioelectron.* **25**, 2543 (2010).

[51] N. Gao, T. Gao, X. Yang, X. Dai, W. Zhou, A. Zhang, and C. M. Lieber, Specific detection of biomolecules in physiological solutions using graphene transistor biosensors, *Proc. Natl. Acad. Sci. USA* **113**, 14633 (2016).

[52] C. Phetsouphanh *et al.*, Immunological dysfunction persists for 8 months following initial mild-to-moderate SARS-CoV-2 infection, *Nat. Immunol.* **23**, 210 (2022).

[53] C. Cervia *et al.*, Immunoglobulin signature predicts risk of post-acute COVID-19 syndrome, *Nat. Commun.* **13**, 446 (2022).

[54] F. Schedin, A. K. Geim, S. V. Morozov, E. W. Hill, P. Blake, M. I. Katsnelson, and K. S. Novoselov, Detection of individual gas molecules adsorbed on graphene, *Nat. Mater.* **6**, 652 (2007).

[55] W. Yuan and G. Shi, Graphene-based gas sensors, *J. Mater. Chem. A* **1**, 10078 (2013).

[56] O. Leenaerts, B. Partoens, and F. M. Peeters, Adsorption of H₂O, NH₃, CO, NO₂, and NO on graphene: A first-principles study, *Phys. Rev. B* **77**, 125416 (2008).

[57] IPCC, *Climate Change 2021: The Physical Science Basis* (Cambridge University Press, Cambridge, 2021).

[58] J. Dai, J. Yuan, and P. Giannozzi, Gas adsorption on graphene doped with B, N, Al, and S: A theoretical study, *Appl. Phys. Lett.* **95**, 232105 (2009).

[59] C. Cazorla, The role of density functional theory methods in the prediction of nanostructured gas-adsorbent materials, *Coord. Chem. Rev.* **300**, 142 (2015).

[60] K. R. Nemade and S. A. Waghuley, Chemiresistive gas sensing by few-layered graphene, *J. Electron. Mater.* **43**, 2767 (2014).

[61] D. Chen, J. Xu, Z. Xie, and G. Shen, Nanowires assembled SnO₂ nanopolyhedrons with enhanced gas sensing properties, *ACS Appl. Mater. Interfaces* **3**, 1158 (2011).

[62] J. L. Johnson, A. Behnam, S. J. Pearson, and A. Ural, Hydrogen sensing using Pd-functionalized multi-layer graphene nanoribbon networks, *Adv. Mater.* **22**, 4877 (2010).

[63] G. Ko, H.-Y. Kim, J. Ahn, Y.-M. Park, K.-Y. Lee, and J. Kim, Graphene-based nitrogen dioxide gas sensors, *Curr. Appl. Phys.* **10**, 1002 (2010).

[64] R. T. Yang, *Gas Separation by Adsorption Processes* (Butterworths, Boston, 1987).

[65] Y. Tang, W. Chen, C. Li, L. Pan, X. Dai, and D. Ma, Adsorption behavior of CO and NO on h-BN monolayer decorated with Pd: a DFT study, *Appl. Surf. Sci.* **475**, 786 (2019).

[66] U.S. Environmental Protection Agency, NAAQS Table, <https://www.epa.gov/criteria-air-pollutants/naaqs-table> (2024).

[67] X. Chen, X. Tan, H. Li, and W. Zhang, Pt decorated graphene as a promising candidate for NO gas sensor: a first-principles study, *J. Mol. Model.* **25**, 169 (2019).

[68] Y. Zhang, D. Zeng, and C. Xie, Noble metal-decorated graphene-based gas sensors and their applications, *Adv. Mater. Interfaces* **8**, 2100311 (2021).

[69] S. Borini, R. White, D. Wei, M. Astley, S. Haque, E. Spigone, N. Harris, J. Kivioja, and T. Ryhänen, Ultrafast graphene oxide humidity sensors, *ACS Nano* **7**, 11166 (2013).

[70] H. Bi, K. Yin, X. Xie, J. Ji, S. Wan, L. Sun, M. Terrones, and M. S. Dresselhaus, Ultrahigh humidity sensitivity of graphene oxide, *Sci. Rep.* **3**, 2714 (2013).

[71] N. Agmon, The Grotthuss mechanism, *Chem. Phys. Lett.* **244**, 456 (1995).

[72] A. D. Smith, K. Elgammal, F. Niklaus, A. Delin, A. C. Fischer, S. Vaziri, F. Forsberg, M. Råsander, H. Huber, and M. C. Lemme, Resistive graphene humidity sensors with rapid and direct electrical readout, *Nanoscale* **7**, 19099 (2015).

[73] V. M. Pereira, A. H. Castro Neto, and N. M. R. Peres, Tight-binding approach to uniaxial strain in graphene, *Phys. Rev. B* **80**, 045401 (2009).

[74] G. Gui, J. Li, and J. Zhong, Band structure engineering of graphene by strain: First-principles calculations, *Phys. Rev. B* **78**, 075435 (2008).

[75] T. M. G. Mohiuddin *et al.*, Uniaxial strain in graphene by Raman spectroscopy: *G* peak splitting, Grüneisen parameters, and sample orientation, *Phys. Rev. B* **79**, 205433 (2009).

[76] Z. H. Ni, T. Yu, Y. H. Lu, Y. Y. Wang, Y. P. Feng, and Z. X. Shen, Uniaxial strain on graphene: Raman spectroscopy study and band-gap opening, *ACS Nano* **2**, 2301 (2008).

[77] L. Sun, Q. Li, H. Ren, Q. W. Shi, J. Yang, and J. G. Hou, Strain effect on energy gaps of armchair graphene nanoribbons, *J. Chem. Phys.* **129**, 074704 (2008).

[78] Y. Lu and J. Guo, Band gap of strained graphene nanoribbons, *Nano Res.* **3**, 189 (2010).

[79] S. K. Ameri, P. K. Singh, and S. Sonkusale, Three dimensional liquid gated graphene field effect strain sensor, arXiv:2107.10818 (2021).

[80] J. Zhao, C. He, R. Yang, Z. Shi, M. Cheng, W. Yang, G. Xie, D. Wang, D. Shi, and G. Zhang, Ultra-sensitive strain sensors based on piezoresistive nanographene films, *Appl. Phys. Lett.* **101**, 063112 (2012).

[81] F. Guinea, M. I. Katsnelson, and A. K. Geim, Energy gaps and a zero-field quantum Hall effect in graphene by strain engineering, *Nat. Phys.* **6**, 30 (2010).

[82] N. Levy, S. A. Burke, K. L. Meaker, M. Panlasigui, A. Zettl, F. Guinea, A. H. Castro Neto, and M. F. Crommie, Strain-induced pseudo-magnetic fields greater than 300 tesla in graphene nanobubbles, *Science* **329**, 544 (2010).

[83] T. Ando, Theory of electronic states and transport in carbon nanotubes, *J. Phys. Soc. Jpn.* **74**, 777 (2005).

[84] K. S. Novoselov *et al.*, Room-temperature quantum Hall effect in graphene, *Science* **315**, 1379 (2007).

[85] K. C. Fong and K. C. Schwab, Ultrasensitive and wide-bandwidth thermal measurements of graphene at low temperatures, *Phys. Rev. X* **2**, 031006 (2012).

[86] J. Yan *et al.*, Dual-gated bilayer graphene hot-electron bolometer, *Nat. Nanotechnol.* **7**, 472 (2012).

[87] C. B. McKittrick, D. E. Prober, and M. J. Rooks, Electron-phonon cooling in large monolayer graphene devices, *Phys. Rev. B* **88**, 075442 (2013).

[88] H. Xu, Z. Zhang, and L.-M. Peng, Measurements and microscopic model of quantum capacitance in graphene, *Appl. Phys. Lett.* **98**, 133122 (2011).

[89] T. Fang, A. Konar, H. Xing, and D. Jena, Carrier statistics and quantum capacitance of graphene sheets and ribbons, *Appl. Phys. Lett.* **91**, 092109 (2007).

[90] L. Spietz, K. W. Lehnert, I. Siddiqi, and R. J. Schoelkopf, Primary electronic thermometry using the shot noise of a tunnel junction, *Science* **300**, 1929 (2003).

[91] J. Crossno, J. K. Shi, K. Wang, X. Liu, A. Harzheim, A. Lucas, S. Sachdev, P. Kim, T. Taniguchi, K. Watanabe, T. A. Ohki, and K. C. Fong, Observation of the Dirac fluid and the breakdown of the Wiedemann-Franz law in graphene, *Science* **351**, 1058 (2016).

[92] A. Lucas and K. C. Fong, Hydrodynamics of electrons in graphene, *J. Phys.: Condens. Matter* **30**, 053001 (2018).

[93] K. A. Ritter and J. W. Lyding, The influence of edge structure on the electronic properties of graphene quantum dots and nanoribbons, *Nat. Mater.* **8**, 235 (2009).

[94] M. Evaldsson, I. V. Zozoulenko, H. Xu, and T. Heinzel, Edge-disorder-induced Anderson localization and conduction gap in graphene nanoribbons, *Phys. Rev. B* **78**, 161407(R) (2008).

[95] E. R. Mucciolo, A. H. Castro Neto, and C. H. Lewenkopf, Conductance quantization and transport gaps in disordered graphene nanoribbons, *Phys. Rev. B* **79**, 075407 (2009).

[96] V. Schroeder *et al.*, Carbon nanotube chemical sensors, *Chem. Rev.* **119**, 599 (2019).

[97] K. Liu *et al.*, Evolution of interlayer coupling in twisted molybdenum disulfide bilayers, *Nat. Commun.* **5**, 4966 (2014).

[98] S. Goossens *et al.*, Broadband image sensor array based on graphene-CMOS integration, *Nat. Photonics* **11**, 366 (2017).

[99] J. Dauber, A. A. Sagade, D. Ober, K. Watanabe, T. Taniguchi, D. Neumaier, and C. Stampfer, Ultra-sensitive Hall sensors based on graphene encapsulated in hexagonal boron nitride, *Appl. Phys. Lett.* **106**, 193501 (2015).

[100] H. J. Yoon, D. H. Jun, J. H. Yang, Z. Zhou, S. S. Yang, and M. M.-C. Cheng, Carbon dioxide gas sensor using a graphene sheet, *Sens. Actuators B* **157**, 310 (2011).